Title
Oceanic plateau of the Hawaiian mantle plume head subducted to the uppermost lower mantle

Journal
Science, 370(6519)

ISSN
0036-8075

Authors
Wei, Songqiao Shawn
Shearer, Peter M
Lithgow-Bertelloni, Carolina
et al.

Publication Date
2020-11-20

DOI
10.1126/science.abd0312

Peer reviewed

Oceanic plateau of the Hawaiian mantle plume head subducted to the uppermost lower mantle (≤ 96 characters)

Short title (≤ 40 characters): Hawaiian plume head in the lower mantle

S. Shawn Wei[1]*, Peter M. Shearer[2], Carolina Lithgow-Bertelloni[3], Lars Stixrude[3], and Dongdong Tian[1]

[1] Department of Earth and Environmental Sciences, Michigan State University, MI 48824, USA.

[2] Cecil H. and Ida M. Green Institute of Geophysics and Planetary Physics, Scripps Institution of Oceanography, University of California, San Diego, La Jolla, CA 92093, USA.

[3] Department of Earth, Planetary, and Space Sciences, University of California, Los Angeles, CA 90095, USA.

*Correspondence to: S. Shawn Wei (swei@msu.edu)

Abstract (≤ 125 words)

The Hawaiian-Emperor seamount chain that includes the Hawaiian volcanoes is created by the Hawaiian mantle plume. Although the mantle plume hypothesis predicts an oceanic plateau produced by massive decompression melting during the initiation stage of the Hawaiian hotspot, the fate of this plateau is unclear. We discovered a megameter-scale portion of thickened oceanic crust in the uppermost lower mantle west of the Sea of Okhotsk by stacking seismic waveforms of *SS* precursors. We propose that this thick crust represents a major part of the oceanic plateau that was created by the Hawaiian plume head about 100 Ma ago and subducted 20–30 Ma ago. Our discovery provides temporal and spatial clues of the early history of the Hawaiian plume for future plate reconstructions.

One sentence summary (≤ 150 characters):

The oceanic plateau created by the Hawaiian mantle plume subducted into the Kamchatka Trench and reached the lower mantle beneath Siberia.

While earthquakes and volcanism at plate boundaries are well explained with the theory of plate tectonics, explaining intra-plate hotspot volcanoes requires the mantle plume hypothesis (*1, 2*). This hypothesis posits deep-rooted and relatively fixed plumes of hot material upwelling through the mantle from the deep Earth and accounts for the age-progressive surface expression known as the Hawaiian-Emperor seamount chain. As the Pacific Plate moves northwest (*3, 4*), the newest volcanoes are found in Hawaii to the southeast, and the oldest seamounts are near the Kamchatka-Aleutian trench junction in the northwest. The ~47 Ma bend of the seamount chain is usually attributed to a change in the Pacific plate motion (*5*). The history of the Hawaiian-Emperor seamount chain is critical for understanding Earth's interior evolution and plate tectonics. In the classical view, a mantle plume consists of a large head (>2,000 km across) and a thin tail (~200 km wide) (*6*). The plume head generates a large igneous province (LIP), such as the Ontong-Java oceanic plateau or the Deccan Traps. The plume tail creates an age-progressive intra-plate volcanic chain. Several efforts have been made to associate ancient LIPs to hotspot volcanoes (*7*). For instance, the Deccan Traps are considered to result from the head of the Reunion mantle plume surfacing more than 68 Ma ago (*8*). However, the fate of the Hawaiian mantle plume head and resulting oceanic plateau is unknown due to the debatable early history of the Hawaiian-Emperor seamount chain.

The Hawaiian-Emperor seamount chain entered the Kamchatka subduction zone based on a variety of plate reconstructions (*3, 4*). One proposal places this event as the cause of the cusp between the Kurile-Kamchatka and the Aleutian-Alaska trenches (*9*). The subduction of the seamounts generates arc lavas with geochemical signatures similar to oceanic island basalts on the Kamchatka Peninsula (*10*). The oldest surface portion of the Hawaiian-Emperor chain, the Meiji Guyot (older than 81 Ma) and Detroit Seamount (76–81 Ma) (*11*) are about to subduct into the Kamchatka Trench (Figure 1). But whether the older parts of the seamount chain, particularly the plume head, also subducted into the deep mantle or stayed on Earth's surface is debated (*12-14*). The fate of the Hawaiian plume head is critical to the origin of the mantle plume, which provides a temporal constraint on the longevity and persistence of chemical characteristics of Earth's deep mantle. Furthermore, the subduction of the expected oceanic plateau caused by the Hawaiian plume head may have changed plate motions. *Niu et al.* (*12*) proposed that the collision of this oceanic plateau with the Kamchatka Trench was responsible for the Pacific Plate reorientation that resulted in the 47-Ma bend in the Hawaiian-Emperor chain.

More importantly, the fate of this oceanic plateau is critical for understanding the role of oceanic plateaus in building continental lithosphere and in mantle convection. Due to their excess crustal thickness and volume, oceanic plateaus are thought to be more difficult to subduct than individual seamounts (*15*). Because the Yakutat terrane southeast of Alaska is the only oceanic plateau that is currently undergoing subduction (*16*), whether oceanic plateaus were commonly subducted in the past is unclear. By analyzing ophiolitic basalts in Kamchatka, *Portnyagin et al.* (*14*) proposed that the Hawaiian plume head, or at least part of it, was accreted to the forearc of Kamchatka. This mechanism provides an important way to grow continental crust (*7*). In contrast, a seismic study of *P*-to-*S* waves converted at seismic discontinuities (receiver functions) in South America suggests that an oceanic plateau with a thickness of at least 13–19 km has subducted to ~100-km depth and is responsible for the Pampean flat slab (*17*). Geodynamic models also show oceanic plateaus can subduct into the upper mantle, resulting in slowing down subduction (*18*), forming a flat slab (*19*), elevating surface topography (*20*), and generating dynamic uplift (*21*). Compared to subducting normal oceanic crust with a thickness of 6–7 km, the input of thick oceanic plateaus might also change, at least locally, mantle composition and dynamics.

Although mantle plume conduits have been successfully imaged using seismic tomography with dense datasets (*22*), oceanic plateaus potentially subducted into the lower mantle have a 20–40 km crustal thickness that is smaller than the resolution in most tomographic studies. Due to a lack of data, the tomography resolution in northeastern Siberia is particularly low in both global (*23*) and regional (*24*) images. Seismic reflected waves are more sensitive to sharp boundaries and provide a more effective tool to detect small-scale compositional heterogeneities in the deep mantle. Many seismic reflectors in the lower mantle have been imaged globally and attributed to segments of subducted crust (*25-27*). But ancient oceanic plateaus have not been detected in the lower mantle, in part due to the limited data coverage in regions they are expected.

We stacked *SS* precursors (*SdS*) from 45 years of global seismic data to detect seismic reflectors in the lower mantle (*28*). The *SdS* seismic phase is the underside *S* wave reflection off the *d*-km discontinuity, which arrives before the surface-reflected *SS* phase (Figure S1A). Because *SS* precursors sample the midpoints between earthquakes and seismic stations, they provide good data coverage for remote regions and are widely used to image seismic discontinuities in the upper and mid mantle (*29*). Besides the major seismic discontinuities extending globally, previous observations detected many smaller-scale reflectors using *SS* or *PP* precursors (*26, 30*).

We focus on a seismic reflector observed at ~810-km depth west of the Sea of Okhotsk, which was previously detected by limited data of *PP* precursors (*30*). The reflector has a width on the order of 1,000 km and a depth varying from 780 to 820 km across (Figure 2). When compared to global tomography models (*23*), the 810-km reflector appears to coincide with the

Kamchatka slab, which is the ancient Pacific Plate subducted along the Kamchatka Trench (Figure 3B). Due to the limited resolution of tomography models, determining whether the reflector is above or at the slab surface (top interface) is challenging. The exact shape of this 810-km reflector is unclear because of the wide Fresnel zone (~1,000 km across) and the low horizontal resolution of *SS* precursors. Additionally, determining the absolute reflector depth and topography relies on the seismic velocity in the upper mantle. With different 3-D mantle velocity models, the average depth of the 810-km reflector varies from 780 to 830 km depending on the choice of model, and its topography also changes from flat to elevated in the center by 30 km (Figure S2 and Figure S3). The seismic signal *S810S* corresponding to the 810-km reflector has an apparent amplitude as strong as that of the *S660S* signal for the 660-km discontinuity. The absolute amplitude of *S810S* is influenced by incoherent stacking and seismic attenuation effects that are difficult to constrain (*28*). Therefore, we conclude that this megameter-scale reflector marks an *S*-wave impedance (product of density and *S*-wave velocity) increase at 780–820 km depths on the same order of magnitude of the impedance increase across the 660-km discontinuity.

In certain regions, we observe an azimuthal dependence of *S810S* in which the signal is only ~~observable~~ detectable along certain azimuths (Figure S4A). This dependence raises the question of whether the *S810S* signal is caused by near-source or near-receiver structures rather than a reflector beneath the midpoints (*31*). However, tests of this possibility confirm the existence of the 810-km reflector west of the Sea of Okhotsk, partly because our observation results from thousands of seismograms with a variety of focal mechanisms (*28*). Although 3-D heterogeneity near sources or receivers may contaminate the *S810S* signals with *PPPS* and *PPPPS* signals from the radial component, the energy contribution should be negligible because the similar *PS* and

PPS waves are too weak to detect on the transverse component (Figure S5E). The azimuthal dependence may also suggest azimuthal anisotropy and small-scale heterogeneity that are difficult to determine conclusively due to our limited data and resolution. Nevertheless, tests of possible scattering artefacts generated by distant 3-D structures indicate that only a near-midpoint reflector is a plausible explanation for the *S810S* observations (*28*).

The 810-km reflector is surprising as it requires dramatic increases in density and *S*-wave velocity. The surface of a flat and cold slab is a natural candidate to explain the reflector. Synthetic waveform modeling shows that either a moderately fast-velocity slab underneath a sub-660 low-velocity zone (LVZ) or a high-velocity slab is required to generate an *S810S* signal similar to our observation (Figure S6). By taking uncertainties of the *S810S* amplitude into account, conservative estimates lead to a 2% velocity reduction for the sub-660 LVZ or a 4% velocity increase within 5 km across the slab surface. However, neither the LVZ nor the ultra-high-velocity anomaly appears in any seismic tomography model and we cannot explain them with thermal variations. In addition, the coherence of the *S810S* observations suggests that the 810-km reflector is nearly flat with a dip angle smaller than 2° within a megameter-wide area (Figure S7 and Figure S8). Such a smooth and flat slab, although often a feature in conceptual models, is unlikely to be a realistic geometry in the mantle. For reference, the Pampean flat slab extends only ~300 km laterally at a depth of ~100 km before dipping into the deep Earth (*17*). Therefore, a simple slab model that is purely controlled by temperature cannot explain our observation.

This flat 810-km reflector could alternatively be caused by a pressure-dominated mineral phase transition. We used a thermodynamic simulation package (HeFESTo) (*32, 33*) to calculate density and *S*-wave velocity profiles of mantle minerals for a variety of bulk compositions along various 1-D thermal profiles (*28*). The mantle composition can be represented by pyrolite, a synthetic rock with the chemical composition of the upper mantle that reaches equilibrium. On the other hand, the mantle is hypothesized as a mechanical mixture of two end-members of mantle differentiation, basalt and harzburgite, that never reaches equilibrium (*34*). With an identical bulk chemical composition, an equilibrium assemblage (pyrolite) and a mechanical mixture of basalt and harzburgite have different phase assemblages and therefore different mineralogical compositions and seismic velocities (*34*). A pyrolytic or harzburgite composition can produce a 660-km discontinuity corresponding to the olivine transition (ringwoodite to bridgmanite and ferropericlase) but with no obvious signal at ~810 km depth (Figure S9). In contrast, a basaltic composition can produce a strong *S810S* signal corresponding to the garnet transition (majorite to bridgmanite) but a small *S660S* signal. If the mantle is a mechanical mixture of basalt and harzburgite, we expect to observe the olivine transition at ~660 km depth due to harzburgite and the garnet transition at ~810 km depth because of the basaltic component. The predicted *S810S* signal is much weaker than the observation even if the basalt fraction (*f*) is 30%, which is much higher than the fraction of 18% suggested for the entire mantle (*34*). Therefore, an equilibrium assemblage of pyrolytic composition or a mechanical mixture of basalt and harzburgite cannot explain the observed *S810S* signal.

A more realistic model is represented by a flat slab at 800–950 km depth with a basaltic crust ~~and~~ overriding on a depleted (harzburgite) slab mantle in the pyrolytic ambient mantle (*35*). Although seismic impedance decreases from the ambient mantle to the slab crust, it increases from the crust to the slab depleted mantle. More importantly, majorite garnet in the slab crust may transform to bridgmanite near 810 km depth, producing a sharp increase in seismic impedance (*28*). The impedance changes in a model with a normal crustal thickness of 6 km are not resolvable by long-period *SS* precursors with the vertical resolution of 30–50 km in the uppermost lower mantle (Figure S10A). In contrast, we obtain a strong *S810S* signal if we assume an oceanic plateau with a 35-km thick crust, which is comparable to the crust of the Ontong-Java Plateau (*36*). This *S810S* signal results from the combination of all impedance changes from the slab surface to Moho (Figure 4). If the oceanic plateau is 20-km thick, the *S810S* signal is still detectable but with a weaker amplitude (Figure S10B). Furthermore, the density profile of the slab crust crosses that of the ambient mantle due to the majorite-bridgmanite transition, suggesting that the slab crust, regardless of its thickness, is neutrally buoyant at the depths of 800–835 km. We cannot assess if the slab crust has been detached from the downgoing slab mantle, as suggested by geodynamic models (*37*), because a model with an orphan slab crust can also produce a detectable *S810S* signal (Figure S10C). Nevertheless, the thick crust of the subducted oceanic plateau, roughly as wide as the Ontong-Java Plateau, probably has been floating in the mantle at 800–835 km depth since it reached these depths due to the neutral buoyancy. This explains the large dimension of the flat slab at a nearly constant depth in the uppermost lower mantle. The possible topographic changes of the 810-km reflector may be caused by thermal and thickness variations of the oceanic plateau.

By comparing with seismic tomographic models and exploring all possible geodynamic and mineralogical explanations, we conclude that the 810-km reflector we observed most likely indicates a megameter-scale thickened crust subducted to the lower mantle. Because this thick crust is on the trajectory of the Hawaiian-Emperor seamount chain (Figure 1), we propose that it is a major portion of the oceanic plateau associated with the head of the Hawaiian mantle plume. Because oceanic plateaus are small compared to the volume of oceanic crust, the subduction of these plateaus will not bias our estimate of the mantle bulk composition. However, this process can lead to localized enrichment of basalt in the mantle and locally alter the slab buoyancy, slowing down subduction (*18*) and contributing to the flattening of slabs above the 660-km discontinuity. If we assume a constant subduction rate of 75 mm/yr and a slab dip angle of 50° above the flat part (*38*), this oceanic plateau subducted into the Kamchatka Trench about 20–30 Ma ago. The subduction of the oceanic plateau is apparently much younger than the bend of the Hawaiian-Emperor seamount chain, and therefore not related to the change in the Pacific plate motion ~47 Ma ago (*5*). Previous studies suggest that the collision between the Ontong Java Plateau and the northern Australian plate margin 6 Ma ago caused a series of plate tectonics events, including the counterclockwise rotation of the Pacific plate (e.g., *39*). The subduction of this Hawaiian plume oceanic plateau temporally coincides with a kink of the Hawaiian-Emperor chain east of Midway Island. However, the causality is unclear, partially because the East Pacific Rise collided with the North America plate around the same time. ~~Similarly~~On the other hand, the subduction of the Pampean flat slab about 10 Ma ago did not cause any dramatic plate reorganization. Further studies with more observations are needed to examine the relationship between oceanic plateau subduction and plate reorganization.

Plate reconstruction models using different mantle reference frames with moving hotspot frames suggest that the Hawaiian hotspot moved from the Izanagi Plate to the Pacific Plate about 100 Ma ago if the hotspot existed earlier (*3, 4, 40, 41*). If the Hawaiian plume head surfaced on the Izanagi Plate, the oceanic plateau would have been subducted into the Aleutian Trench towards the North Pole more than 70 Ma ago, inconsistent with our observation. Therefore, we believe that the oceanic plateau associated with the Hawaiian plume head was formed on the Pacific Plate no earlier than 106 Ma. This estimate is consistent with the 93–120-Ma old ophiolitic basalts in Kamchatka that were produced by the Hawaiian plume and accreted to the

Kamchatka forearc much later (*14*). Given the available plate reconstruction models (*3, 4, 40, 41*)~~(*3, 4*)~~, we hypothesize that the Hawaiian plume head surfaced about 100 Ma ago to create a megameter-scale oceanic plateau at the Izanagi-Pacific Ridge (Figure S11). As the mid-ocean ridge spread, the oceanic plateau broke into two parts, and the Izanagi part moved northward and subducted into the ancient Aleutian Trench about 72 Ma ago. On the other hand, before the Pacific part of the oceanic plateau subducted into the Kamchatka Trench, its eastern margin might also have encountered the Aleutian Trench and a possible subduction zone between the Kula and Kronos Plates (*42*). There are discrepancies between the plate reconstruction models and our inferences regarding the subduction time and the present position of the Pacific part of the oceanic plateau. This direct comparison is challenging because the detailed history of this plateau highly depends on the initial location and migration rate of the Izanagi-Pacific ridge. ~~But~~ However, our observations provide critical constraints for future plate reconstructions.

Acknowledgments

We thank L. Colli, S. Dorfman, M.J. Krawczynski, R. Maguire, A. McNamara, W. Panero, J. Wu, and X. Yue for constructive discussions and Y. Liu for valuable help using GPlates (*43*). Three anonymous reviewers and the editor provided helpful comments to improve the manuscript. We thank the 2019 Interior of the Earth Gordon Research Conference for providing opportunities of interdisciplinary collaboration. We also appreciate the free access of GPlates for plate reconstructions. Seismic data analysis was supported in part through computational resources and services provided by the Institute for Cyber-Enabled Research at Michigan State University. **Funding:** This work was made possible by NSF grants OCE-1842989 to S.S.W., EAR-1620251 to P.M.S., EAR-1900633 to C.L-B., and EAR-1853388 to L.S. S.S.W. and D.T. were also supported by the MSU Geological Sciences Endowment. C. L-B. was further supported by the Louis B. and Martha B. Slichter Endowment for Geosciences. **Author contributions:** S.S.W., with the help of P.M.S. and D.T., analyzed the seismic data. C.L.B. and L.S. conducted the thermodynamic simulations of mantle minerals. D.T. downloaded and maintained the seismic database. S.S.W. took the lead in writing the manuscript, and all authors discussed the results and edited the manuscript. **Competing interests:** The authors declare no competing interests. **Data and code availability:** We use 1987–2018 data from seismic networks AC, AE, AF, AI, AK, AT, AU, AV, BE, BL, BX, C1, CB, CD, CH, C, CM, CN, CT, CU, CZ, DK, DR, DW, EI, G, GB, GE, GT, HL, HT, IC, II, IP, IU, JP, KN, KO, KP, KR, KS, KZ, LX, MC, MI, MM, MM, MS, MX, MY, NA, ND, NJ, NO, NR, NU, OE, OV, PL, PM, PR, PS, RM, RV, S, SV, TA, TM, TR, TT, TW, UK, US, VE, WI, and WM. All raw seismic data are available at the Data Management Center of Incorporated Research Institutions for Seismology (www.iris.edu/dms/nodes/dmc). We also use 1995–2018 F-net data from the Japan National Research Institute for Earth and Science and Disaster Resilience (https://doi.org/10.17598/NIED.0005). The thermodynamic simulation package HeFESTo (*32, 33*) is available at https://github.com/stixrude/HeFESToRepository, and Table_270914 includes all parameters used for the thermodynamic simulations. GPlates is available at https://www.gplates.org.

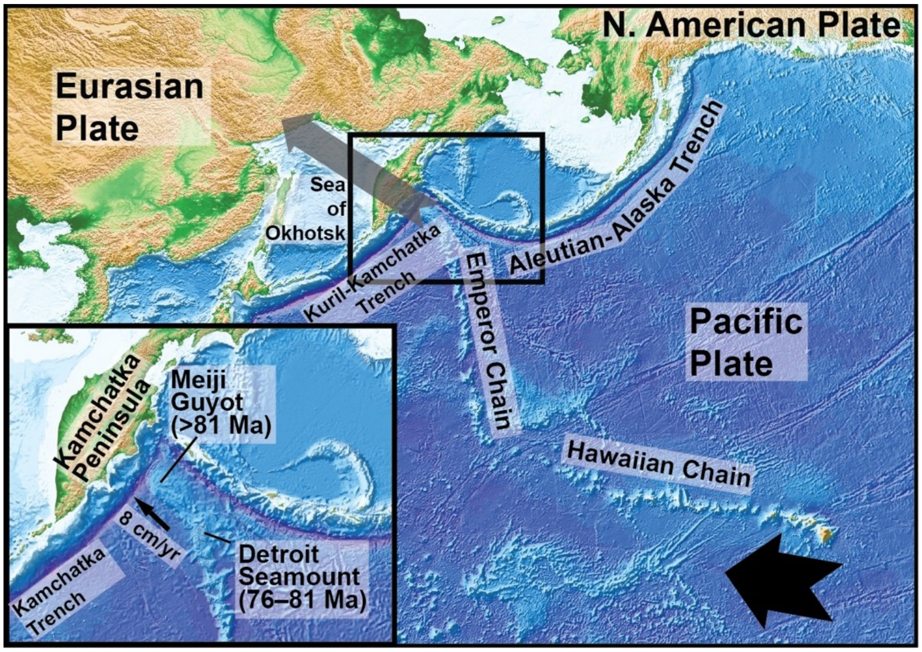

Figure 1. Topographic-bathymetric map (*44*) of the northern Pacific Ocean and Northeast Asia. The bold black arrow indicates the current motion of the Pacific Plate at Hawaii relative to the Hawaiian plume, whereas the gray arrow represents the approximate trajectory of the Hawaiian-Emperor seamount chain into the Kamchatka subduction zone based on plate reconstructions (*3, 4*). Inset shows the Kamchatka region where the oldest seamounts (Meiji Guyot and Detroit Seamount) of the Hawaiian-Emperor chain are about to subduct into the Kamchatka Trench at a speed of 8 cm/yr.

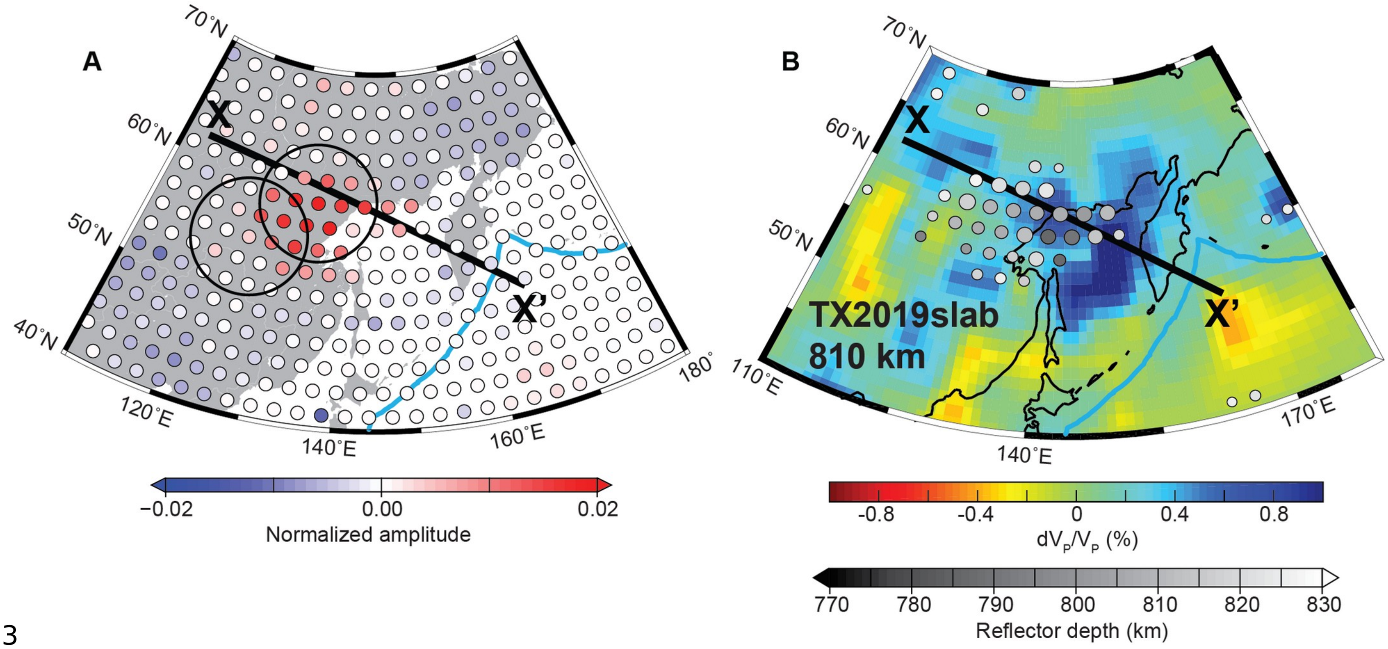

Figure 2. Maps of the 810-km reflector compared with velocity tomography. (A) Map of amplitudes (above the 95% confidence level) of stacked *SS* precursor waveforms at 810 km depth in the Siberia-Okhotsk-Kamchatka region. The *SS* precursor amplitude is normalized to the *SS* amplitude in the same cap. Red circles show the high amplitude of *S810S*, indicating the 810-km reflector. *SS* precursors are stacked in overlapping bouncepoint caps of 5° radius and 2° spacing. The black open circles outline the actual area of caps, which are represented by small solid circles at their centers and color-coded by amplitude. Note that the lateral resolution of our data is about 1,000 km, which is comparable with the size of each cap and the Fresnel zone width. The black curve indicates the cross-section X-X' in Figure 3. Blue curves illustrate convergent plate boundaries (*45*). (B) Depth of the 810-km reflector in caps superimposed on the TX2018slab *P*-wave tomography model (*23*) at 810 km depth. The reflector depth is shown by the grayscale in caps where it is detected. Circle sizes are scaled to emphasize reliable caps according to the depth uncertainty. In caps where the 810-km reflector is less evident due to low

amplitude, its depth has larger uncertainties. Caps with depth uncertainties greater than 10 km are omitted.

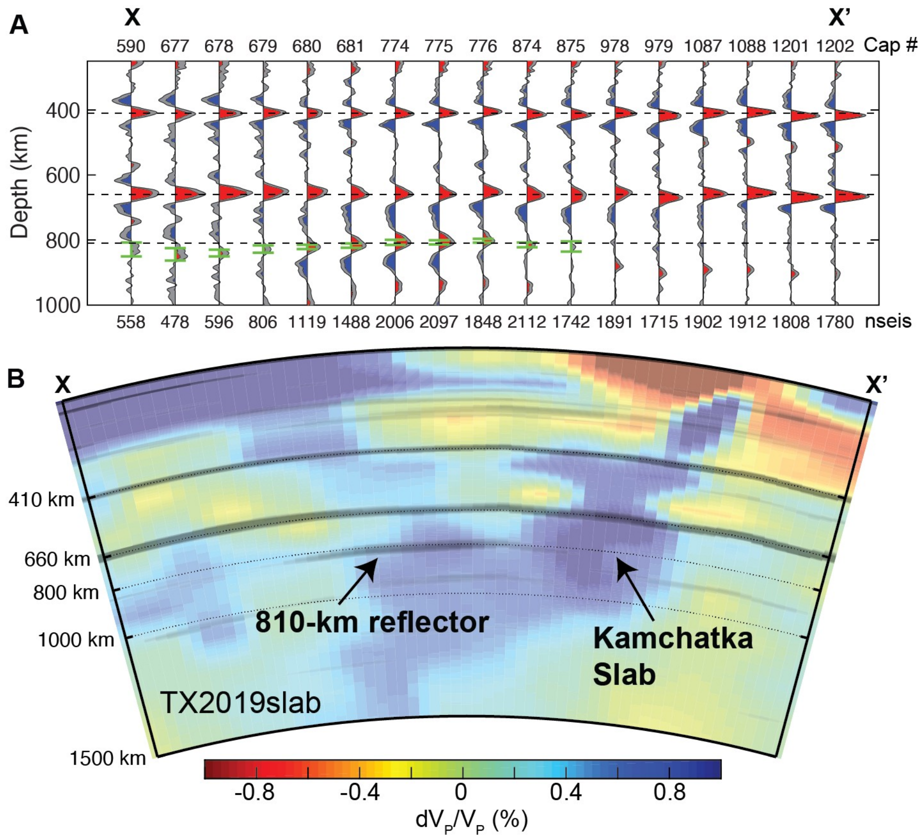

Figure 3. Cross-section of apparent discontinuities and reflectors along the cross-section shown in Figure 2A. (A) Stacked *SS* precursors observed in overlapping caps of 5˚ radius and 2˚ spacing. All seismograms are converted to the depth domain, stacked, and then corrected for 3-D velocity heterogeneity based on the TX2019slab *S*-wave velocity model (*23*). Red and blue indicate robust positive and negative signals above the 95% confidence levels, respectively, whereas grey shows the stack uncertainty (2-sigma). Black dashed lines show depths of 410, 660, and 810 km. The cap indices are on the top, whereas the numbers on the bottom show the numbers of seismograms stacked in those caps. A strong peak appears at about 810 km depth in certain caps. Green error-bars indicate the depth of the 810-km reflector in each cap where it is detected. Weak positive signals at greater depths are artifacts resulting from interfering seismic phases (topside reflections off the 410- and 660-km discontinuities, i.e., Ss410s and Ss660s)

rather than *SS* precursors. Similar cross-sections with different depth corrections based on other *S*-wave tomography models are shown in Figure S2. (B) Apparent discontinuities and reflectors (dark stripes) from *SS* precursor stacks superimposed on the TX2018slab *P*-wave tomography model (*23*). All positive signals shown in (A) are interpolated and shown as dark stripes, whereas all negative signals are omitted. Similar cross-sections superimposed on other *P*-wave tomography models are shown in Figure S3.

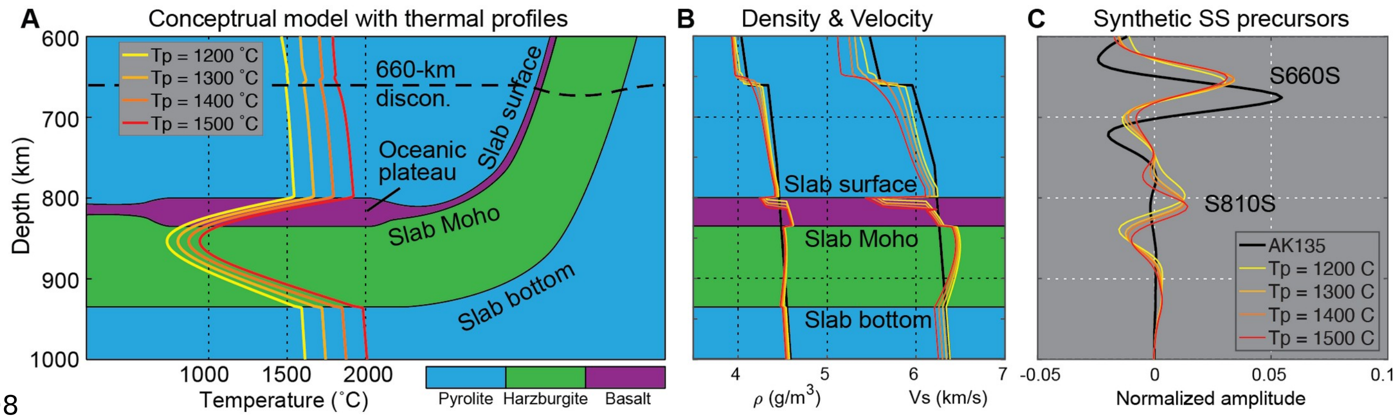

Figure 4. The garnet transition in an oceanic plateau in the lower mantle can explain the observed *S810S* signal. (A) A conceptual model of the Kamchatka slab subducted into the lower mantle. Blue, green, and purple colors represent pyrolitic, harzburgite, and basaltic compositions, respectively. The oceanic plateau has a crustal thickness of 35 km, whereas the other parts of the oceanic crust are 6-km thick. Yellow to red curves show the thermal profiles across the flat slab with a variety of potential temperatures (T_P). (B) Density and *S*-wave velocity profiles corresponding to the thermal profiles in (A). Black curves indicate the AK135 reference model (*46*). Note that the density profiles of the slab crust cross that of the reference model at 800–830 km depths due to the majorite-bridgmanite transition, indicating that the oceanic crust is neutrally buoyant along all thermal profiles. (C) Synthetic *SS* precursor waveforms corresponding to the density and velocity profiles in (B). The *S810S* signal is strong enough to be observed along all thermal profiles. Note that we do not try to fit the exact waveform because of the large uncertainties of thermodynamic parameters of minerals and the *S810S* amplitude.

Supplementary Materials

Materials and methods

Data processing and stacking

Since *SS* precursor waveforms are usually weak and buried in noise, stacking is required to enhance the signal. We compile the largest dataset of *SS* precursors recorded at global permanent broadband stations, the USArray TA stations, and the Japan F-net stations from 1973 to 2018, and stack the waveforms in a similar manner to *Shearer* (*29*). The dataset is restricted to earthquakes shallower than 75 km depth to reduce complications owing to depth phases. Each transverse-component seismogram is band-pass filtered between 15 and 100 s (first-order Butterworth, zero-phase shift). Then the *SS* phase is automatically picked by searching for the maximum amplitude around the predicted *SS* arrival time according to the IASP91 model (*47*). The polarity of each seismogram is flipped if necessary so that the *SS* peak amplitude is always larger than its negative sidelobes. We discard seismograms with signal-to-noise ratios of *SS* lower than 3 and restrict the source-receiver distance to 124–176° to avoid interference from the *Ss660s* phase. This quality control process results in about 20,000 seismograms sampling the Siberia-Okhotsk-Kamchatka region shown in Figure 2. Each trace is normalized and aligned to the maximum *SS* amplitude and then converted from time to depth based on the IASP91 model. Each trace thus becomes amplitude as a function of depth. All depth-domain traces are stacked in overlapping bouncepoint caps of 5° radius and 2° spacing globally, as this configuration can avoid artificially abrupt changes due to the choice of caps (*48*). However, it is important to emphasize that our technique has lateral resolution of only about 1,000 km despite a finer grid of caps with 2° spacing. The uncertainties of the stacked waveforms and the reflector depth are estimated using a bootstrap resampling method (*49*), where we repeat the stacking 200 times using random subsets of the data. Besides the prominent 410- and 660-km discontinuities, a strong positive signal appears at a depth between 800 and 850 km in certain caps (Figure S2A).

After stacking in the depth domain, we apply a depth correction to account for lateral velocity variations in the crust and mantle following the procedure of *Shearer* (*29*). At each bouncepoint cap, we build a 1-D S-wave velocity profile based on the Crust1.0 model (*50*) and a 3-D mantle velocity model, calculate the *SS*–*SdS* differential traveltimes for a series of depths (*d*), and compare them with those using the IASP91 model. The differences in the *SS*–*SdS* differential traveltimes are then converted to depth corrections. We use the TX2019slab (*23*), S40RTS (*51*) and SEMUCB_WM1 (*22*) *S*-wave tomography models to estimate the exact depth of the 810-km reflector. Figure 2, Figure 3, and Figure S2 suggest that the depth of the 810-km reflector varies from 780 to 830 km depending on the *S*-wave velocity structure in the upper mantle. We also plot the *SS* precursor stacks on top of the *P*-wave velocity models because these models have higher resolution than *S*-wave models and show a clear Kamchatka slab. For models with only *P*-wave velocity [MIT-P08 (*52*), GAP-P4 (*53*), and UU-P07 (*54*)], we calculate the *S*-wave velocity based on V_P/V_S ratios from the IASP91 model (*47*). Since only TX2019slab (*23*) includes both *P*- and *S*-wave velocity models, we use these models for our primary results and further discussions.

It is important to measure the slowness of the *S810S* signal because other seismic phases may generate the same stacked waveform if their energy concentrates in a narrow source-receiver range that coincides with *S810S*. We thus stack seismograms in the time domain for bouncepoint cap #744 where a strong *S810S* signal is detected (see Figure S1B for its location). Figure S5A shows 2,664 traces sharing this cap stacked as a function of source-receiver range and aligned to the *SS* phase. A strong positive signal about 50 s earlier than *S660S* is observed at the range of 116–142° (black ellipse), coinciding with the traveltime of *S810S*. Although we also detect other mid-mantle reflectors in a global survey, similar to *Waszek et al.* (*26*), our dataset does not provide wide enough source-receiver ranges to unambiguously determine the slownesses of those reflectors. We thus only focus on the 810-km reflector in the Siberia-Okhotsk-Kamchatka region.

Effects of incoherent stacking

The stacking technique assumes a reference 1-D Earth model. However, discontinuity topography or 3-D upper-mantle velocity structure will cause time shifts that weaken the stack coherence, which reduces the *SdS* amplitude. Seismic attenuation has an opposing effect, as it reduces the *SS* amplitude and broadens its waveform compared to *SdS* owing to extra paths through the upper mantle. When *SS* is used as a reference phase, the normalized *SdS* amplitude is increased by attenuation. Because neither the reflector topography nor the upper-mantle attenuation is well constrained, we do not focus on the amplitude of *S810S* in this study. Instead, the relative amplitude of *S810S* compared to *S410S* and *S660S* provides semi-quantitative insights regarding the sharpness and impedance contrast of the 810-km reflector.

Following *Wei and Shearer* (*48*), we conduct a series of incoherent stacking tests by assuming that the arrival time shifts are caused by the reflector depth variations which have a Gaussian distribution characterized by a standard deviation σ. This experiment shows that the *SdS* amplitude will be halved if $\sigma = 50$ km within a bouncepoint cap due to incoherent stacking (Figure S7A). A similar experiment suggests that if the reflector has a dip angle of 5° within a 10°-wide cap, the *SdS* amplitude will also be halved (Figure S7B). As discussed in the main text, the impedance contrast across the 810-km reflector is likely to be smaller than that across the 660-km discontinuity. Given the fact that *S810S* is as strong as *S660S* in some caps, it is reasonable to assume that the weakening effects of incoherent stacking on *S810S* are less significant than on *S660S*. Therefore, we expect the 810-km reflector to be smoother and flatter than the 660-km discontinuity. In other words, the incoherent stacking experiments suggest that the 810-km reflector is at a nearly constant depth (σ < 20 km) and almost flat with a dip angle smaller than 2° within a megameter-wide area (cap size).

We also experiment with more complex topographies of the 810-km reflector with Kirchhoff migration (*55*). We assume a variety of topographic changes and use the event-station information of Cap #774 to simulate synthetic stacks of *S810S* (Figure S8). The amplitude of *S810S* can be dramatically reduced due to defocusing if the depth perturbation is large. The wavelength of the topographic change appears to be less important in influencing the long-period *SS* precursor waves.

Azimuthal dependence of *S810S*

The azimuthal dependence of *S810S* in certain caps (Figure S4A) is puzzling and suggests the possibility of near-source or near-receiver structures rather than a reflector beneath the midpoints. In particular, seismograms stacked in cap #774 are dominated by rays from Sumatra earthquakes to North American stations with azimuths of 0–60° (Figure S1C). If we restrict data to an azimuthal range of 300–360°, stacks in the time domain show no signal of *S810S* (Figure S5C). *Zheng and Romanowicz* (*31*) analyzed seismic waves from a single earthquake in northern Sumatra and recorded by the USArray TA stations in North America. Their study suggests that the upper-mantle structure beneath North America may generate an artificial double *S660S* signal, similar to the *S810S* signal observed in this study. This is because the 3-D heterogeneities beneath North America may cause energy leakage from the radial to transverse component of seismograms, so that *PPPS* and *PPPPS* phases with similar traveltimes and slownesses can contaminate *SS* precursors.

In order to test the possible contamination of *PPPS* and *PPPPS* phases, we restrict our data to the 2008–2010 TA data and azimuths of 40–60˚. The distributions of stations and azimuths are similar to that were used by *Zheng and Romanowicz* (*31*). The transverse- and radial-component seismograms in cap #774 are stacked as a function of time and source-receiver range (Figure S5). The stacks show that *S810S* is similar to *S660S* and *S410S* on the transverse component, while *PS*, *PPS*, *PPPS*, and *PPPPS* appear on the radial component. It is difficult to directly distinguish *S810S* from the possible leakage of *PPPS* and *PPPPS* to the transverse component due to their similar traveltimes and slownesses. However, a few observations provide insights to the nature of the observed *S810S* signal: (1) Since the traveltime curves of *PPPS* and *PPPPS* are closer at shorter source-receiver ranges, the interference amplitude (negative sidelobe) between these two phases changes systematically with respect to source-receiver range on the radial component. However, *S810S* does not show such a systematic change in amplitude on the transverse component. (2) A strong *PPS* phase is observed on the radial component, whereas no energy appears on the transverse component. Since *PPS* and *PPPS* share similar raypaths in the upper mantle beneath receivers, it is unlikely that substantial leakage of the *PPPS* phase occurs but no *PPS* phase is seen on the radial component. (3) Our observation of *S810S* results from thousands of seismograms with a variety of earthquakes that are different from the single event used by *Zheng and Romanowicz* (*31*). Therefore, we conclude that the *S810S* signal observed here is generated by a reflector beneath the great-circle midpoint, although energy leakage from the radial component may contribute a small amount to the observations.

More importantly, we also observe the *S810S* signal at azimuths of 300–360° in a nearby cap #970 (Figure S4B). This cap is dominated by seismic rays from southwestern Pacific earthquakes to European stations (Figure S1C). The amplitude of *S810S* is smaller than that of *S660S*, suggesting that it is caused by a reflector with a weaker impedance contrast compared to the 660-km discontinuity beneath the midpoints rather than structures near sources or receivers.

An alternative explanation for the azimuthal dependence of *S810S* is azimuthal anisotropy of seismic velocity above or underneath the reflector. However, this cannot explain the different azimuthal dependences in caps #774 and #970. We suspect that this discrepancy partially results from small-scale lateral variations of reflector topography and impedance contrast within each bouncepoint cap. Unfortunately, we do not have sufficient resolution to distinguish lateral heterogeneity from azimuthal anisotropy due to the wide Fresnel zone of long-period *SS* precursors.

In conclusion, we are confident of the existence of the 810-km reflector, although its absolute amplitude is uncertain. The azimuthal dependence of *S810S* may result from azimuthal anisotropy and small-scale heterogeneity that are beyond our resolution, as well as a small contribution from the 3-D heterogeneities near sources or receivers.

Off-midpoint scatterers

SS wave and its precursors *SdS* follow a maximum-time path along the great circle path connecting source and receiver and a minimum-time path orthogonal to the source-receiver azimuth. Therefore, the traveltime differences for reflection points that deviate from the midpoint position form a saddle-shaped surface (Figure S12B). Thus, scatterers on a saddle-shaped surface (iso-time depths) shown in Figure S12B can generate reflected waves with the same traveltime as the *SdS* wave reflected at the midpoint. However, the common midpoint stacking strategy used in this study assumes that the observed *SdS* energy can be mapped exclusively to the midpoint and ignores other possible scatters. To test whether scattering away from the midpoint could generate our observed signal, we plot the locations where scattered waves would arrive with the same traveltime as our observed reflector and compare these locations with the TX2019slab *P*-wave tomography model (Figure S12C and D). There is no obvious velocity increase other than the Kamchatka slab at the midpoint that coincides with the iso-time depth contour. Additionally, systematic experiments in migration processing show that the off-axis scattering does not significantly bias the common midpoint stacking procedure for *SS* precursor data (*55*).

Synthetic waveform modelling

Following *Wei and Shearer* (*48*), we compute synthetic *SdS* waveforms by convolving the reference *SS* phase with discontinuity operators. The discontinuity operators are calculated from reflection coefficients and geometric spreading for a specific model of density and *S*-wave velocity. Since our technique of stacking long-period seismic waves provides limited spatial resolution, and it is challenging to constrain the effects of incoherent stacking and seismic attenuation, we intentionally avoid fitting the observed waveforms wiggle by wiggle. Instead, we focus on generating an *S810S* signal with an amplitude comparable to that of *S660S*. Therefore, geometrical ray theory is sufficiently accurate to capture the main features of interest in our study.

Since the 810-km reflector appears above the Kamchatka slab in all tomographic models (Figure 3 and Figure S3), it is worthwhile to test whether this reflector represents a sharp slab surface (top interface) that is purely controlled by temperature. Figure S6 shows four attempts of modelling *SS* precursor waveform with a horizontal high-velocity zone (slab) in the lower mantle. Either a sub-660 low-velocity zone (LVZ) with a velocity reduction of 3% or an high-velocity slab with a velocity increase of 6% within 5 km across the slab surface is required to produce the observed *S810S* signal (Figure S6A and B). Even if we assume that the observed *S810S* amplitude is overestimated due to the effects of focusing, azimuthal anisotropy, and small-scale heterogeneity, we still need a sub-660 LVZ with a velocity reduction of 2% or an high-velocity slab with a velocity increase of 4% within 5 km across the slab surface to produce an *S810S* amplitude as large as a half of the *S660S* amplitude (Figure S6C and D). However, none of these features appears in any tomographic models, and the sharp velocity increase cannot be explained by a simple thermal model that is governed by heat conduction.

Alternatively, we compute synthetic *SS* precursor waveforms based on thermodynamic simulations of mantle minerals for a variety of compositions (Figure S9). We extract density and *S*-wave velocity profiles from the HeFESTo outputs along adiabatic thermal profiles with a variety of mantle potential temperatures (T_P), calculate synthetic waveforms, and convert them to the depth domain. For a mechanical mixture of basalt and harzburgite, we calculate the elastic properties of the assemblage as the Voigt-Reuss-Hill average of those values of basalt and harzburgite (*56*).

Thermodynamic simulations of mantle minerals

We use the code HeFESTo, which is described in detail in our previous publications (*32, 33*). Briefly, this is a Gibbs free energy minimization code, based on the concept of fundamental thermodynamic relations, that captures phase equilibria and physical properties, including the elastic moduli, self-consistently. The elastic moduli of lithologic assemblages are computed as Voigt-Reuss-Hill averages of the constituent minerals. We adopt compositions of pyrolite, harzburgite, and basalt from our previous work (*34*).

The end-member species and the values of the parameters that describe their thermodynamics are specified in Table_270914 in https://github.com/stixrude/HeFESToRepository. These values are updated from our previous work (*32*) in the following ways. We have replaced the Na-bearing end-member of the garnet phase with the Na-majorite composition; we have added the $NaAlO_2$ end-member to the ferropericlase phase; we have added the sodium-aluminum rich phase (nal); and we have updated parameters of several phases, for example, the regular solution parameters of the Calcium-Ferrite (cf) phase to better describe cf-nal phase relations, and the temperature derivative of the shear modulus of bridgmanite (*57*).

In thermodynamic equilibrium, we find that the transition from a garnet-dominated assemblage to a bridgmanite-dominated assemblage in MORB occurs at 30.2 GPa (810 km depth) along the 1200 ˚C adiabat. This is considerably deeper than what was found in a recent experiment (25 GPa, or 700 km depth) (*58*), that was designed to produce conditions of thermodynamic equilibrium, and that was not considered in our determination of the species parameters used in our HeFESTo calculations. However, the subducted Hawaiian plume head may not be in thermodynamic equilibrium. At the relatively cold temperatures that exist in subducting slabs, the garnet-bridgmanite transition may occur at much greater depths because of kinetic hindrances (*59, 60*). Most of the transition may occur over a relatively narrow depth interval because of a transition from dominantly grain-boundary to dominantly intra-crystalline nucleation that occurs near 800 km depth (*61*). Experimental data on the rate of the garnet to bridgmanite transition are still limited and a fully quantitative treatment of the kinetics is not justified at present. In order to capture the likely effects of kinetics, we therefore interpret our HeFESTo-generated velocity profiles (Figure 4), as approximating the location of the garnet to bridgmanite transition as it would occur in the subducted and kinetically hindered Hawaiian plume head, i.e., near 810 km. We estimate the uncertainty in the density and velocity contrast across the transition to be less than 1%; the sharpness of the transition is consistent with the interpretation of the kinetic data (*60*).

Modelling a flat slab in the lower mantle

A flat slab in the uppermost lower mantle is represented by a basaltic crust and a depleted (harzburgite) slab mantle in the pyrolytic ambient mantle (*35*). We set the slab crustal thick as 6 km for a normal oceanic plate and 35 km for an oceanic plateau, similar to the crustal thickness of the Ontong-Java Plateau (*36*). The slab is modelled as a semi-infinite slab (*62*) with a constant subducting rate of 75 mm/yr and a dip angle of 50° (*38*), and its lithospheric mantle is assumed to be 100-km thick. The thermal condition within the slab temperature is purely controlled by heat conduction. We then build a 1-D thermal profile across the 810-km reflector for each T_P (Figure 4A). In the ambient pyrolitic mantle, temperature follows the adiabatic path. Within the slab lithosphere, we adopt the thermal profile across the slab at 900-km depth because the 810-km reflector would have been at ~900 km depth if the slab is not deflected. Although the slab thermal structure must be more complicated than this simple model, our strategy is capable of capturing the first-order thermal variations given the wide range of T_P. Based on the HeFESTo outputs and a 1-D thermal profile, the 1-D density and *S*-wave velocity profiles for this flat slab model consists of four segments: (1) values of pyrolite above the slab surface, (2) values of a basaltic composition in the slab crust, (3) values of harzburgite in the slab mantle, and (4) values of pyrolite underneath the slab bottom (Figure 4B). Synthetic *SS* precursor waveforms are computed based on these 1-D density and *S*-wave velocity profiles (Figure 4C). We also test different subducting rates (50–100 mm/yr) and dip angles (40–60°) that will systematically change the slab thermal profiles. The choice of these values can change the *S800S* signal depth by ± 5 km without noticeable changes in the signal amplitude.

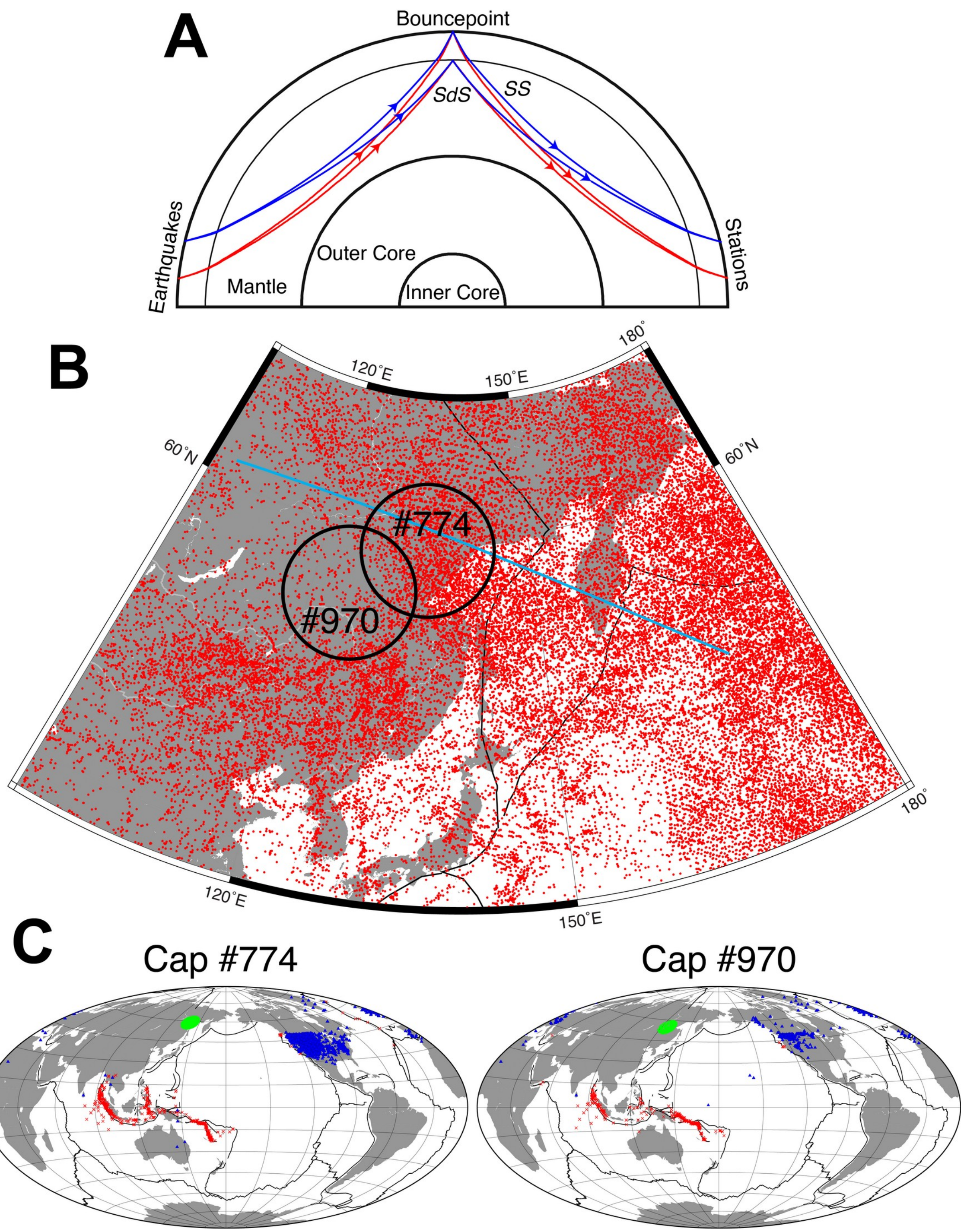

Figure S1. Maps of bouncepoints, stations, and earthquake. (A) Cartoon showing two pairs of *SS* and its precursor (*SdS*) sharing the same bouncepoint for stacking [modified after *Wei and Shearer* (*48*)]. (B) Map of the Siberia-Okhotsk-Kamchatka region and bouncepoints of seismograms (red dots). Black curves show tectonic plate boundaries. Black circles outline caps #774 and #970, in which all seismograms are stacked to produce Figure S4 and Figure S5. (C)

Distribution of events (red crosses), stations (blue triangles), and bounce points (green dots) used for stacking in caps #774 and #970.

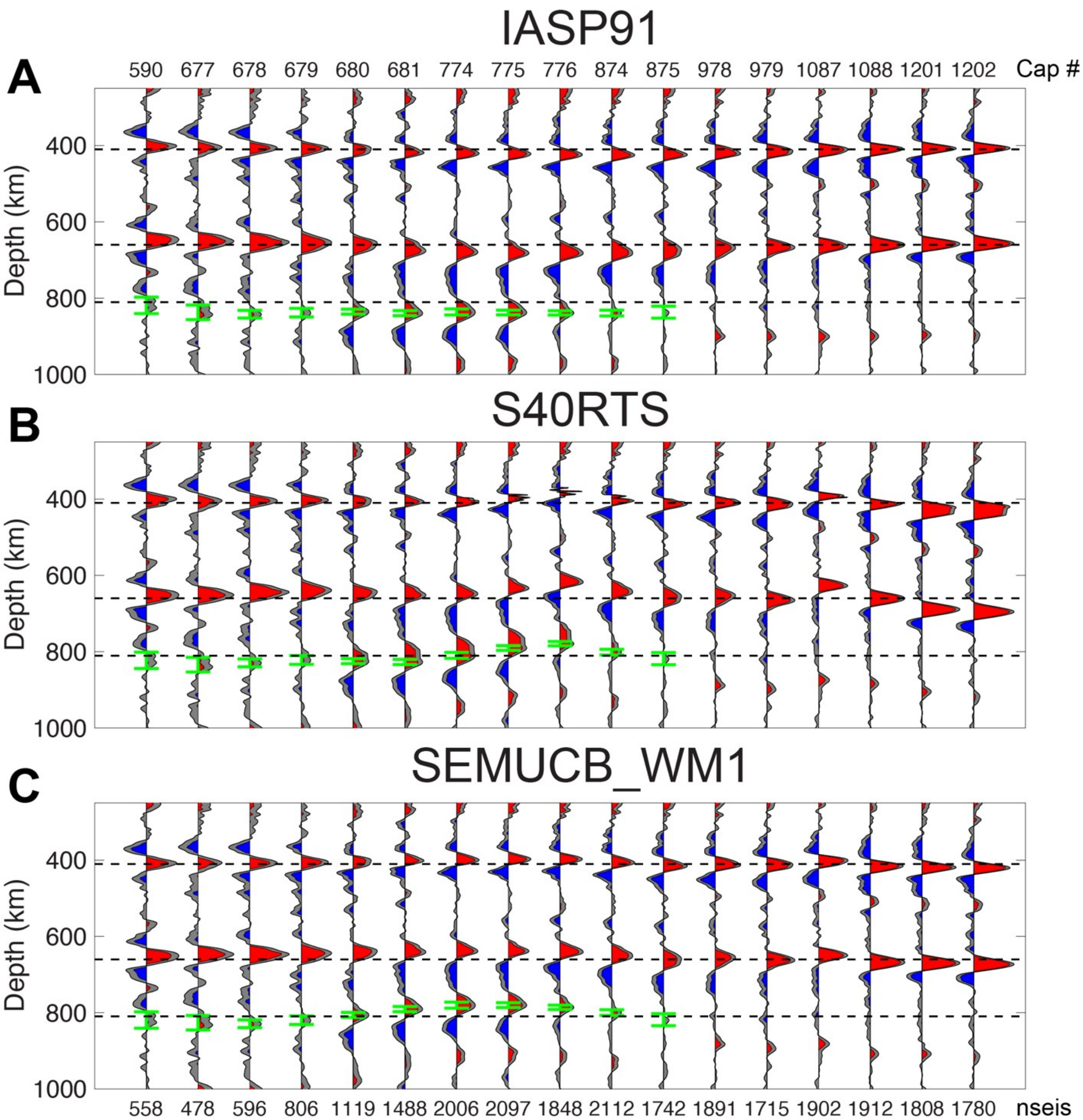

Figure S2. Apparent discontinuities and reflectors from stacked *SS* precursors similar to Figure 3A. All seismograms are converted to the depth domain based on the IASP91 model (*47*), stacked, and then corrected for 3-D velocity heterogeneity based on the S40RTS (*51*) and SEMUCB_WM1 (*22*) *S*-wave tomography models. The 810-km reflector varies from 780 to 830 km after the depth correction.

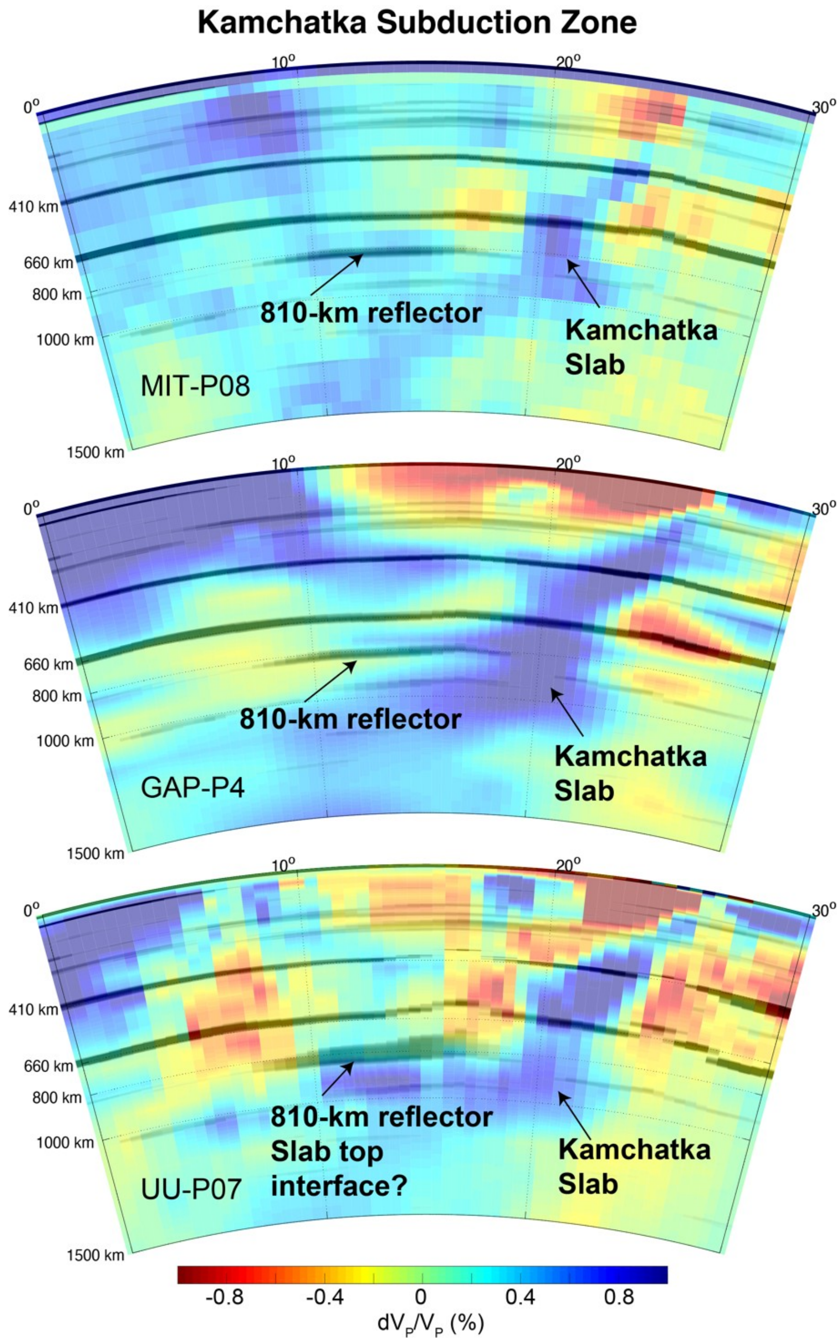
Kamchatka Subduction Zone
MIT-P08
GAP-P4
UU-P07
810-km reflector
Kamchatka Slab
810-km reflector Slab top interface?
410 km
660 km
800 km
1000 km
1500 km
0°
10°
20°
30°
-0.8
-0.4
0
0.4
0.8
dVP/VP (%)

563

Figure S3. Apparent discontinuities and reflectors from *SS* precursor stacks superimposed on different *P*-wave tomography models. These are similar to Figure 3B except that the tomography models are MIT-P08 (*52*), GAP-P4 (*53*), and UU-P07 (*54*). The depths of apparent discontinuities and reflectors are corrected based on the *P*-wave model used and the V_P/V_S ratios from the IASP91 model (*47*).

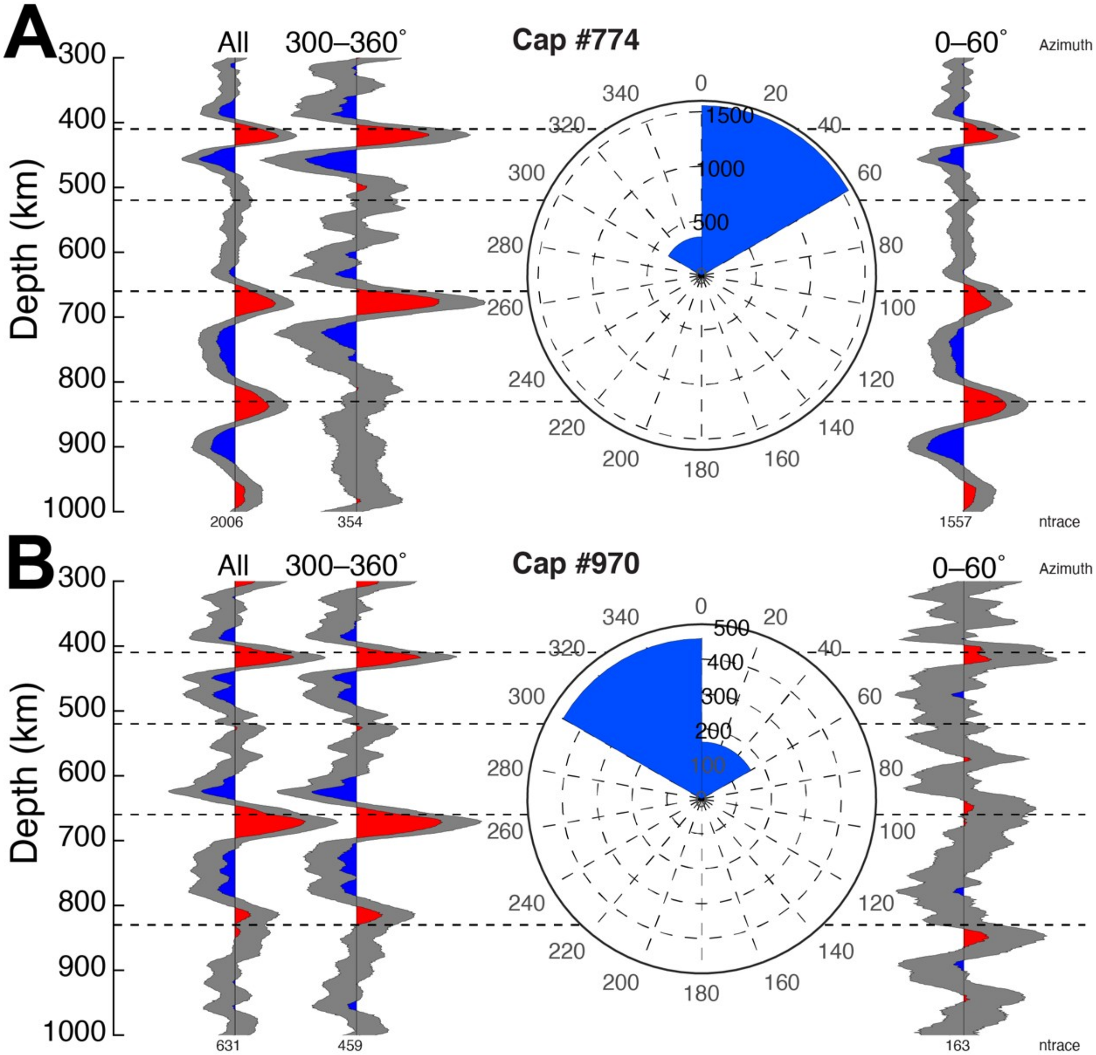

Figure S4. Azimuthal dependence of *S810S* in caps #774 and #970 (black circles in Figure 2). Inset rose diagrams show the azimuthal distribution of seismograms in each cap. The digits on the top are azimuthal ranges, whereas the digits on the bottom show the number of stacked traces. (A) In cap #774, a strong positive signal is observed at ~830 km depth (before the depth correction) with azimuths ranging from 0–60˚ (1,557 seismograms stacked), whereas little signal of this feature is observed at in the azimuthal range of 300–360˚ (354 seismograms stacked). (B) In cap #970, a positive signal is observed at ~850 km (before the depth correction) with azimuths ranging from 0˚–60˚ (163 seismograms stacked), but at ~810-km depth in the azimuthal range of 300˚–360˚ (459 seismograms stacked). This discrepancy may suggest small-scale lateral variations in topography and impedance contrast that are beyond the lateral resolution of our technique.

581

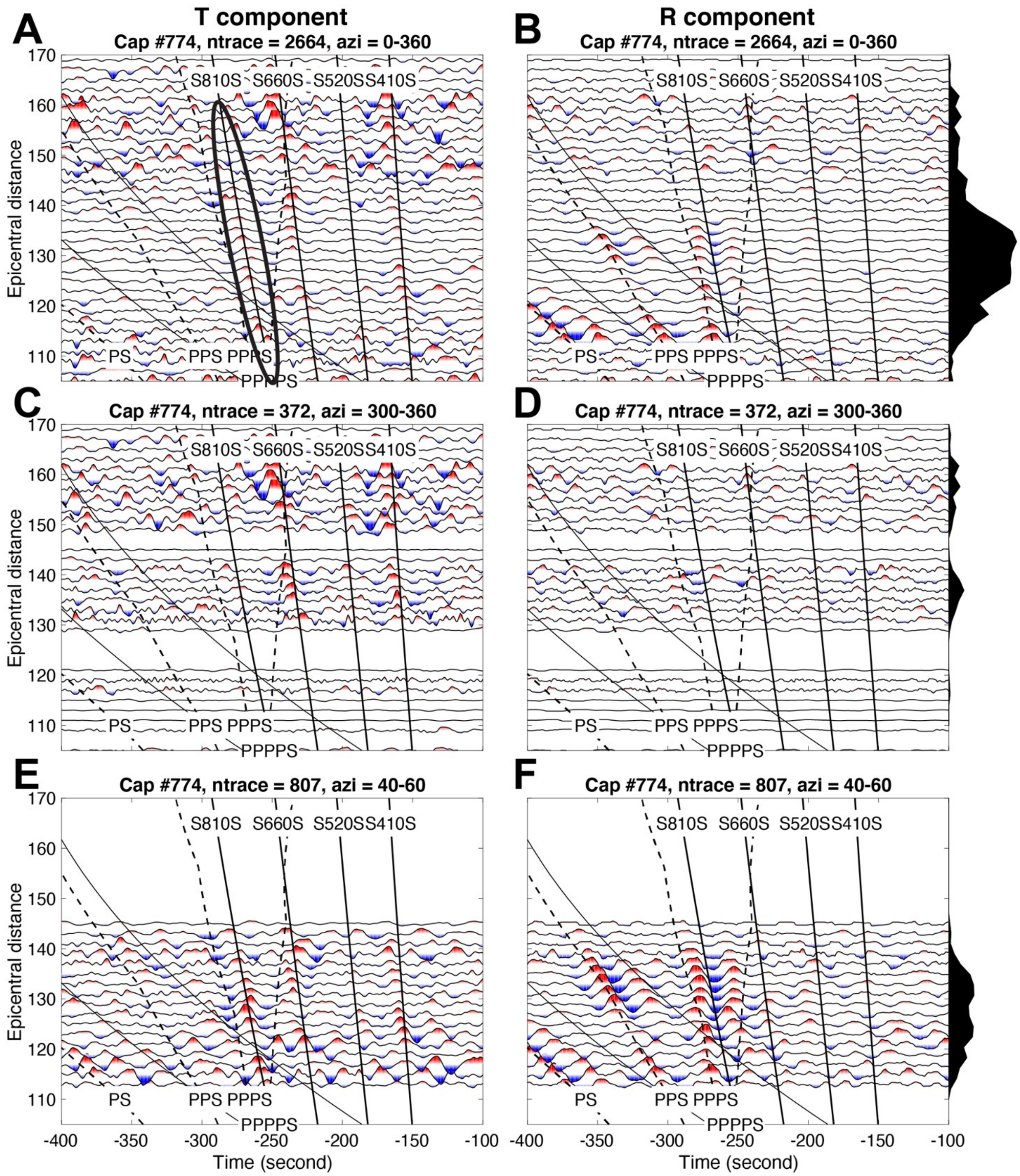

T component
R component
A
B
C
D
E
F
Cap #774, ntrace = 2664, azi = 0-360
Cap #774, ntrace = 372, azi = 300-360
Cap #774, ntrace = 807, azi = 40-60
S810S
S660S
S520S
S410S
PS
PPS
PPPS
PPPPS
Epicentral distance
Time (second)
170
160
150
140
130
120
110
-400
-350
-300
-250
-200
-150
-100

Figure S5. Transverse- and radial-component seismograms stacked in cap #774 aligned to the reference *SS* phase, color-coded by normalized amplitude. Stack amplitude is weighted by the number of traces stacked in each bin of source-receiver range, which is illustrated by the black area on the right. Solid curves indicate phases that are supposed to appear on the transverse component, whereas dashed curves indicate phases that should only be visible on the radial component. (A, C, E) Transverse-component stacks. (E, D, F) Radial-component stacks. (A and B) All available data stacked. A strong positive signal about 50 s earlier than *S660S* is observed at the range of 116˚ to 142˚ (black ellipse), coinciding with the traveltime of a possible 810-km reflector. (C and D) The data is restricted to azimuths of 320–340˚. There is no obvious *S810S* signal on the transverse component. (E and F) The data is restricted to only the 2008–2010 USArray TA data and azimuths of 40–60˚, for direct comparison with *Zheng and Romanowicz* (*31*). The *S810S* signal appears to result from the same mechanism as the *S410S* and *S660S* signals, i.e., horizontal discontinuity or reflector beneath the bounce point. *PS, PPS,* and *PPPS* waves are obvious at the range of 110–136˚ on the radial component. The lack of *PS* and *PPS* signals on the transverse component suggests that there is little energy leakage from the radial to transverse component.

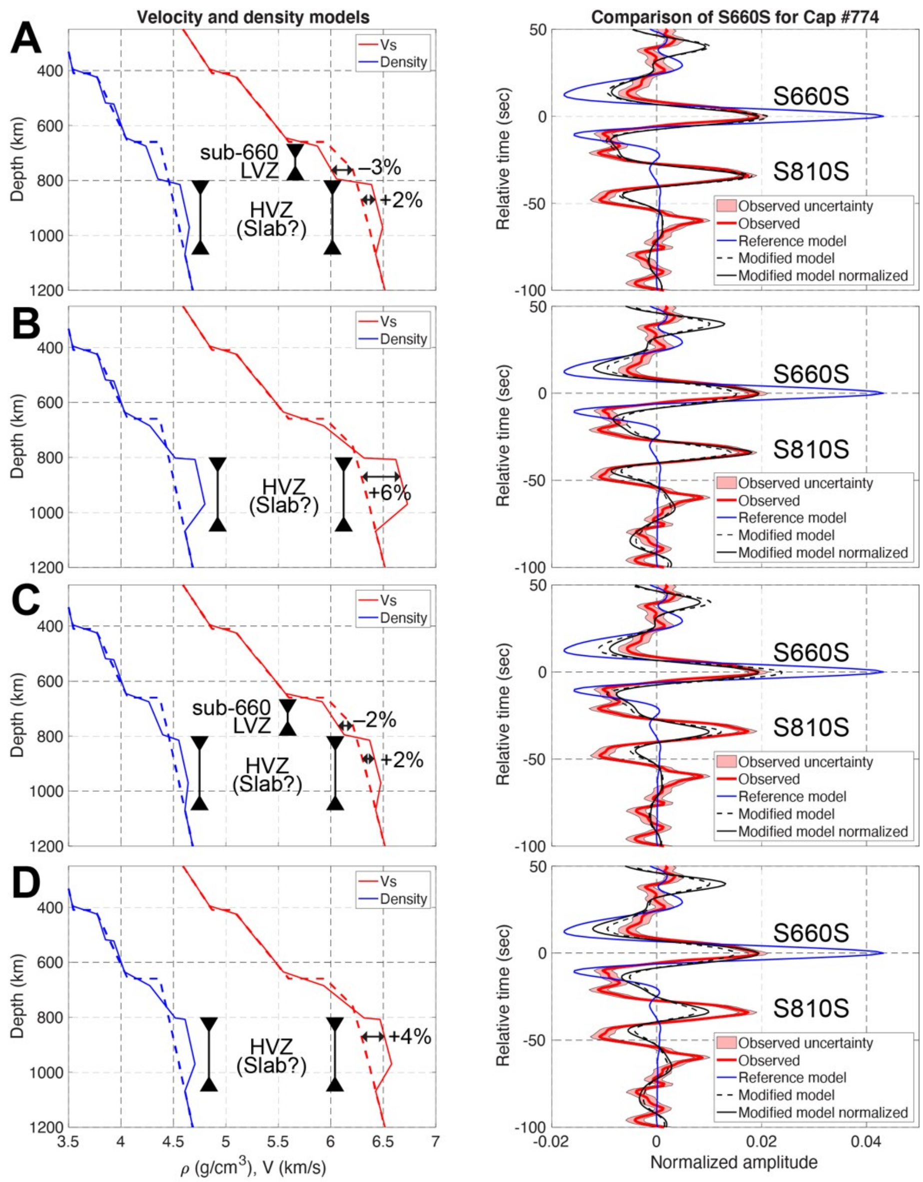

Figure S6. Attempts of modeling *SS* precursor waveforms with a horizontal high-velocity zone (a possible flat slab) in the lower mantle. (Left panels) 1-D profiles of *S*-wave velocity and density across the high-velocity zone (HVZ). Dashed lines indicate the AK135 reference model (*46*). Solid lines show the modified model corresponding to the synthetic waveforms that approximately fit the observations. (Right panels) Observed (red) and synthetic *SS* precursor waveforms. The blue curve shows the synthetic waveform produced by the AK135 model, whereas the black curves (original or amplitude-normalized) corresponding to the modified model fit the observation better. (A and C) Models with a 30-km thick 660-km discontinuity, a sub-660 low-velocity zone (LVZ), and an HVZ at 800–1050 km depths. (B and D) Models without a strong sub-660 LVZ but including a 50-km thick 660-km discontinuity and an HVZ at 800–1050 km depths. The models in (A) and (B) can produce an *S810S* amplitude fitting the observation. If we assume the observed *S810S* amplitude is overestimated due to the effects of focusing, azimuthal anisotropy, and small-scale heterogeneity, the models in (C) and (D) can produce a detectable *S810S* amplitude similar to Figure 4.

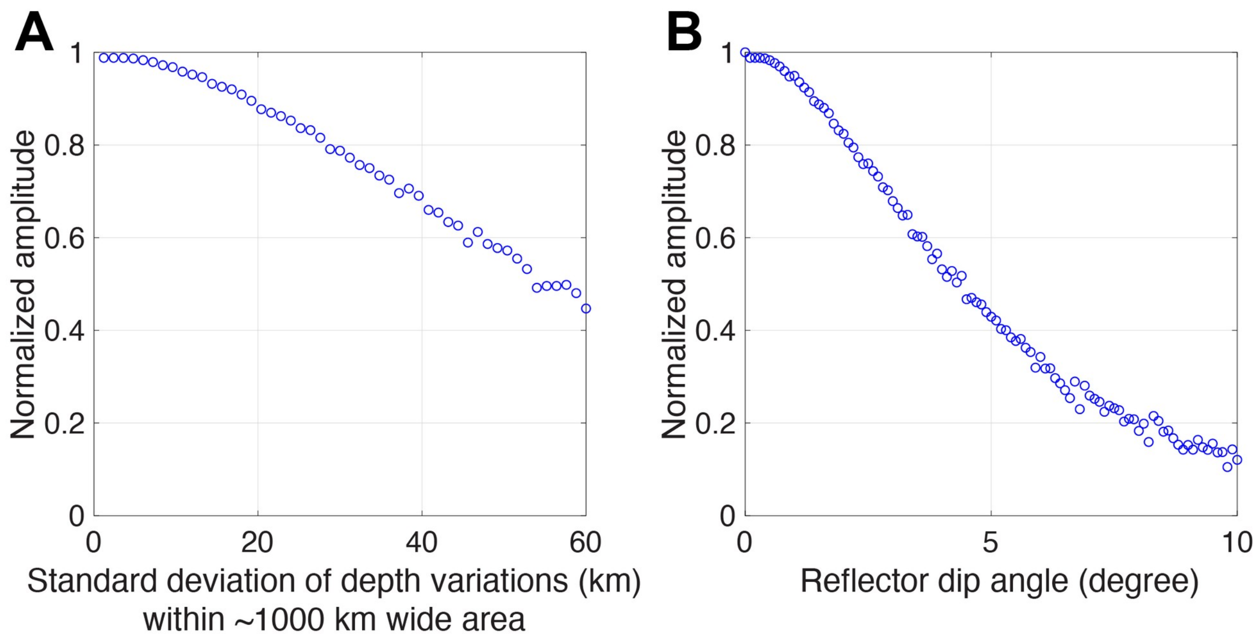

Figure S7. Effects of incoherent stacking. 2,000 identical waveforms are stacked when their traveltimes are not perfectly aligned but follow a Gaussian distribution. (A) The traveltime shifts are caused by the reflector depth variations with a standard deviation σ within a bouncepoint cap (~1,000 km wide). (B) The traveltimes are shifted because of a dipping reflector. The standard deviation of the traveltime shifts is 1/3 of the maximum time variation, which is determined by the reflector dip angle. Tests suggest that a strong reflector detected by our technique should be relatively smooth and flat, with a dip angle smaller than ~2° and depth variations less than ~20 km within a megameter-scale area (cap size).

622

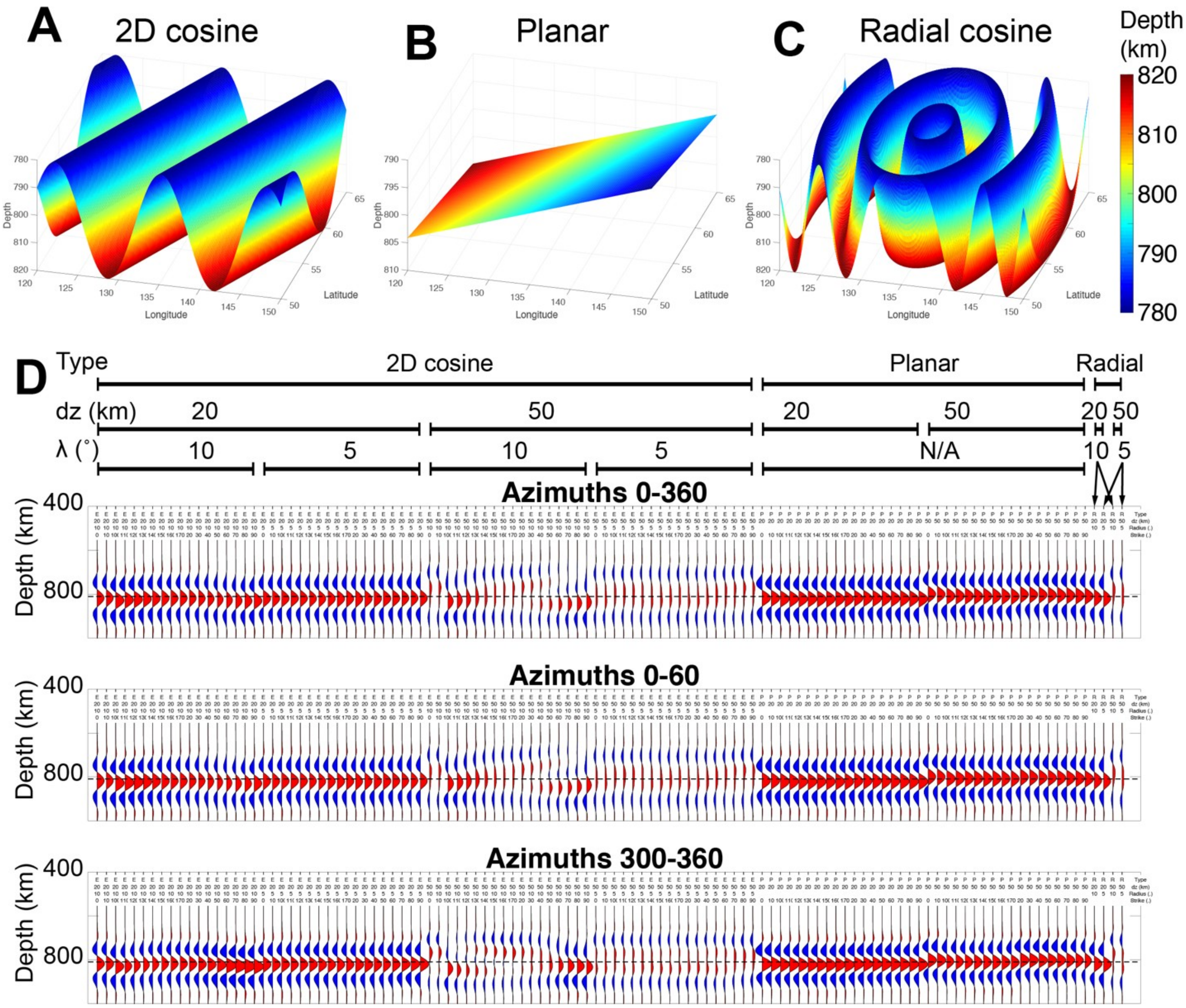

A
2D cosine
B
Planar
C
Radial cosine
Depth (km)
820
810
800
790
780
Depth
Longitude
Latitude
D
Type
2D cosine
Planar
Radial
dz (km)
20
50
20
50
20
50
λ (˚)
10
5
10
5
N/A
10
5
Azimuths 0-360
Azimuths 0-60
Azimuths 300-360
Depth (km)
400
800

Figure S8. Experiments of Kirchhoff migration with various topographies of the 810-km reflector. (A) Assuming the reflector topography follows a 2-D cosine function. (B) Assuming the reflector is planar. (C) Assuming the reflector topography follows a radial cosine function. (D) Synthetic stacks of *S810S* with a variety of topography types, depth perturbations (dz), wavelengths (λ), and strikes. Black dashed lines indicate the 810-km depth.

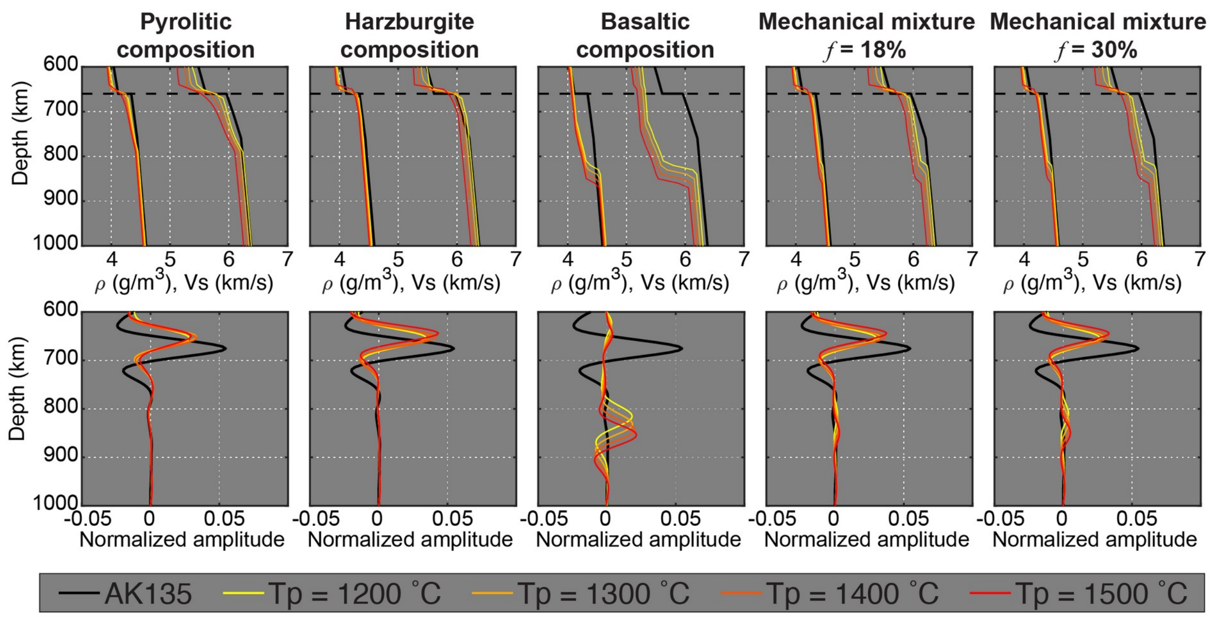

Figure S9. Mineralogical simulation and synthetic waveform modelling. (Upper) Seismic velocity and density profiles with various mantle potential temperatures (T_P) predicted by HeFESTo for a variety of mantle compositions. The elastic properties of a mechanical mixture with a basalt fraction (*f*) are calculated as the Voigt-Reuss-Hill average of that of basalt and harzburgite (*32, 34*). (Lower) Corresponding synthetic *SS* precursor waveforms in the depth domain. Although increasing the basaltic component can amplify the *S810S* signal, it is not sufficient to explain our observation even if f = 30%.

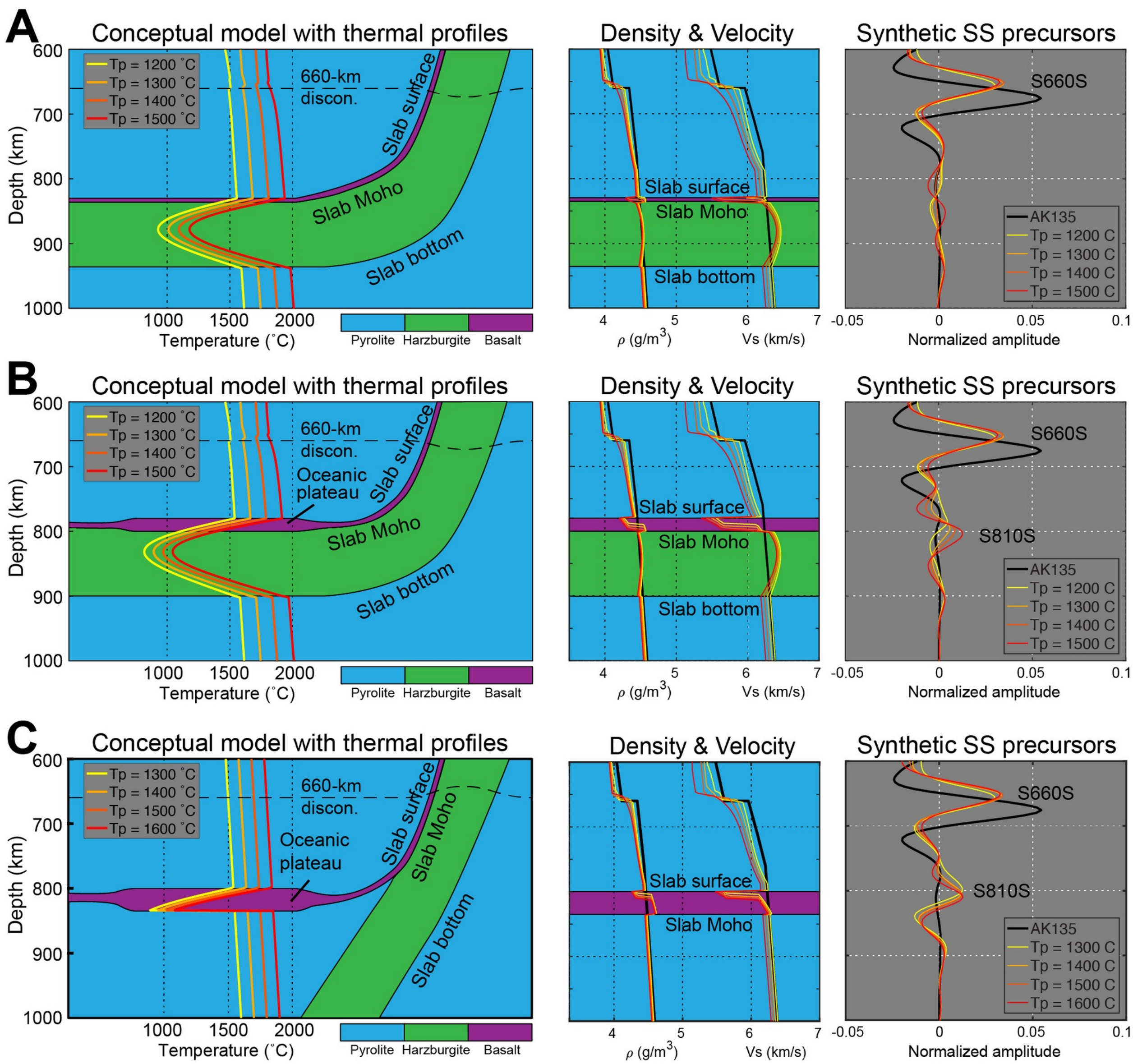

Figure S10. A subducted slab with various crustal thicknesses. (A) A slab without an oceanic plateau. All panels are similar to Figure 4 except that the crustal thickness is consistently 6 km, and the slab surface is at 830-km depth. Consequently, no *S810S* is observable along any thermal profiles. (B) A slab with a 20-km-thick oceanic plateau and the slab surface is at 780-km depth. The *S810S* signal is visible for the warmest scenarios. (C) A slab crust with a 35-km-thick oceanic plateau detached from the downgoing slab mantle. The *S810S* signal is visible along all thermal profiles.

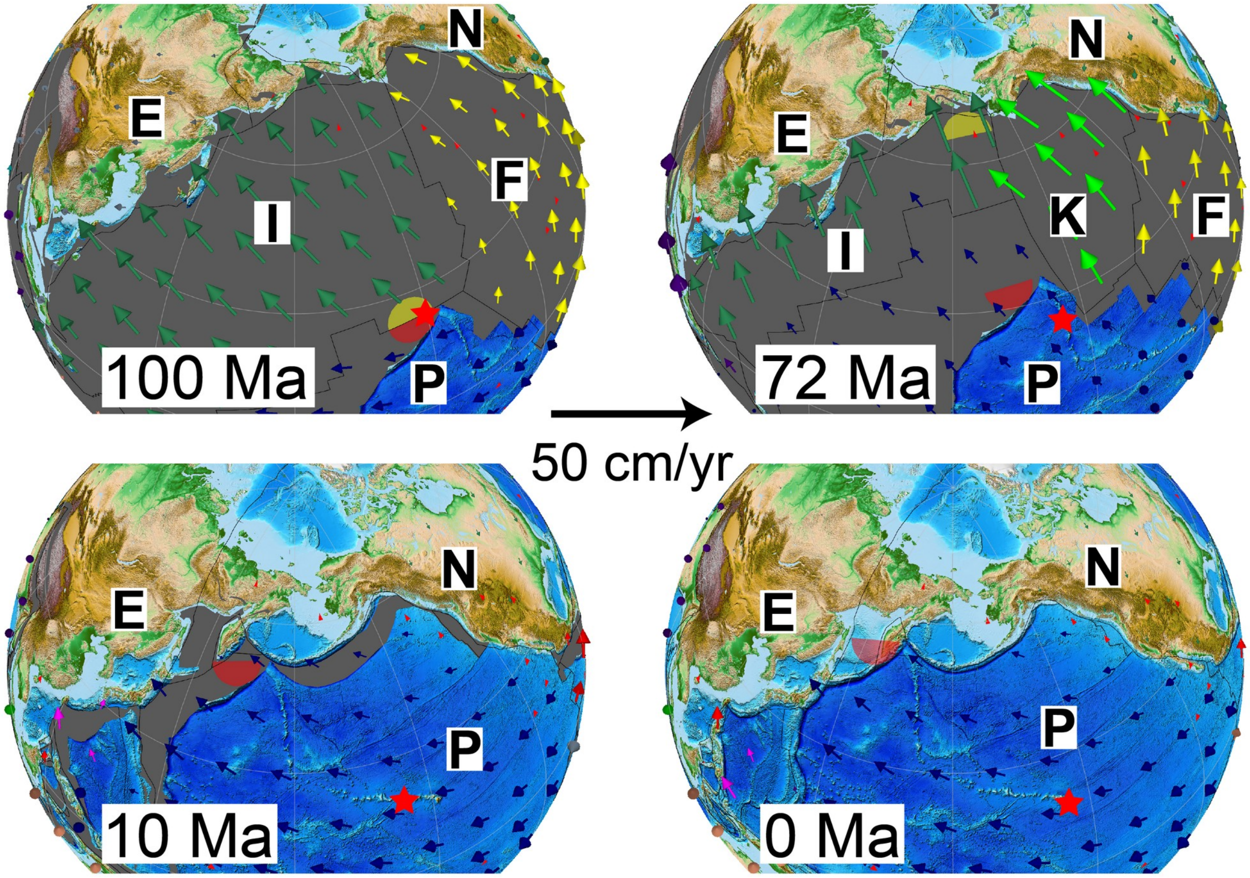

Figure S11. A possible history of the oceanic plateau created by the Hawaiian plume head 100 Ma ago. Plate reconstruction is visualized by GPlates (*43*) ~~with~~ using the model of *Matthews et al.* (*3*) with a mantle reference frame from *Müller et al.* (*40*). Movie S1 shows the amination of this plate reconstruction. Plate reconstruction with a different model (*4*) and hotspot reference frame (*41*). leads to similar results. Major plates are label~~l~~ed: E, Eurasia; F, Farallon; I, Izanagi; K, Kula; N, North American; P, Pacific. The red star indicates the Hawaiian mantle plume. Arrows show plate motion. The red semicircle represents the Pacific part of the oceanic plateau, whereas the yellow semicircle shows the Izanagi part. When the Hawaiian mantle plume surfaced about 100 Ma ago, it created an oceanic plateau at the Izanagi-Pacific Ridge. As the Izanagi-Pacific Ridge spread, the oceanic plateau broke into two parts, and the Izanagi part moved northward and subducted into the ancient Aleutian Trench about 72 Ma ago. The Pacific part of the oceanic plateau started to subduct into the Kamchatka Trench about 10 Ma ago. Note that this time is later than our inferred timeframe (20–30 Ma) based on the 810-km reflector location. Consequently, the Pacific part of the oceanic plateau does not reach Siberia at 0 Ma in this reconstruction model. The discrepancies may imply large uncertainties of the initial location and migration rate of the Izanagi-Pacific ridge.

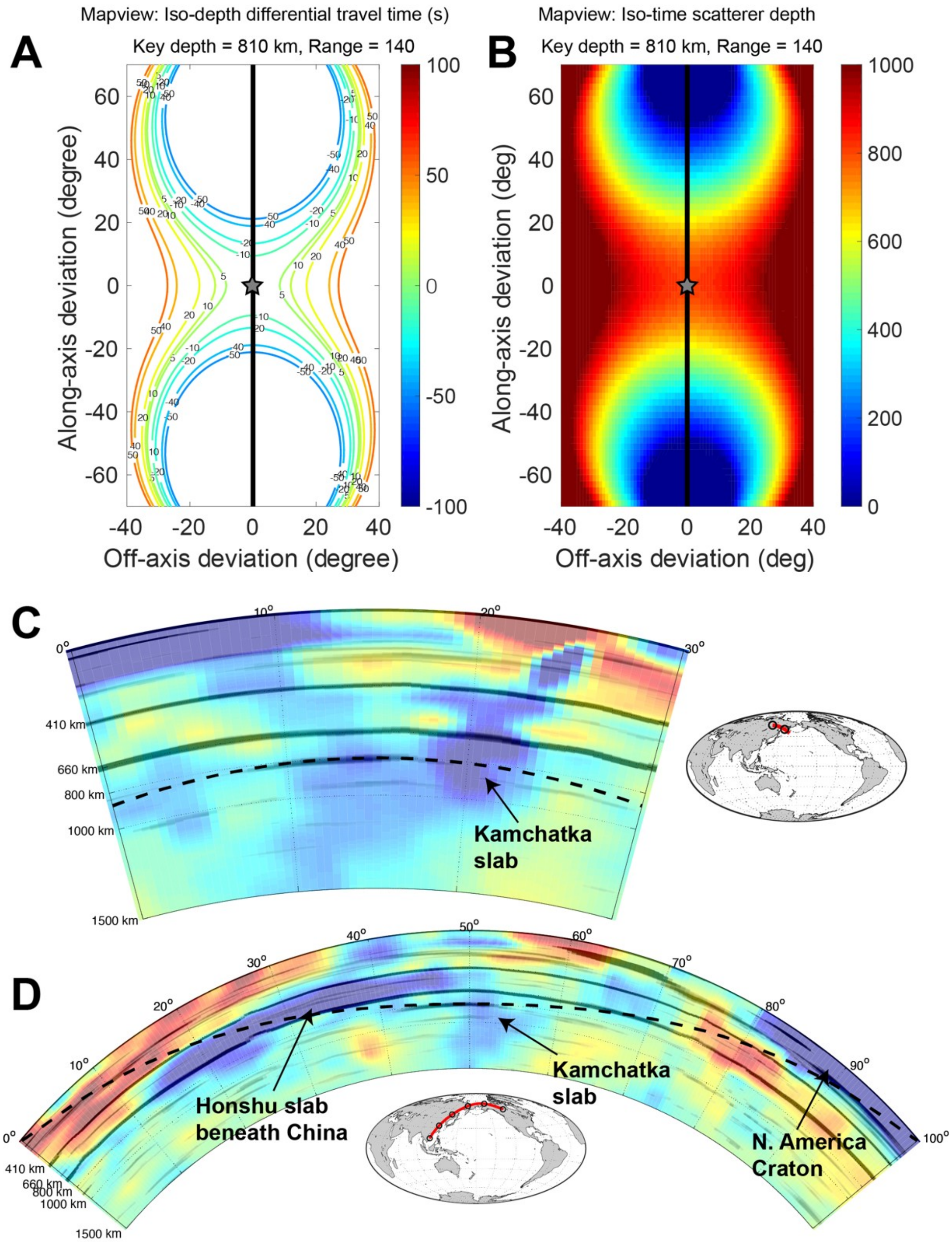

Figure S12. Effects of off-midpoint stacking. (A) Contours of traveltime differences for lateral perturbations to the *S810S* bounce point at 140˚ source-receiver range for a discontinuity or reflector at 810-km depth. The black line indicates the great circle raypath, and the grey star is the midpoint. (B) Iso-time depths of hypothetical point scatterers that produce the same precursor arrival time as a midpoint reflector at 810-km depth, assuming the source-receiver range is 140˚. (C) The iso-time depth contour (black dashed curve) along the cross- section shown in Figure 3b. (D) The iso-time depth contour (black dashed curve) along a cross-section with an azimuth of

50° crossing the 800-km reflector. There is no obvious velocity increase other than the Kamchatka slab coinciding with the iso-time depth contour.

Movie S1. A possible history of the oceanic plateau created by the Hawaiian plume head since 100 Ma. Plate reconstruction is visualized by GPlates (*43*) ~~with~~ using the model of *Matthews et al.* (*3*) with a mantle reference frame from *Müller et al.* (*40*). Red triangles indicate hotspots. Arrows show plate motion. The yellow and red semicircles represent the oceanic plateau on the Izanagi and Pacific Plates, respectively.

References

1. J. T. Wilson, A Possible Origin of the Hawaiian Islands. *Canadian Journal of Physics* **41**, 863-870 (1963).
2. W. J. Morgan, Convection Plumes in the Lower Mantle. *Nature* **230**, 42-43 (1971).
3. K. J. Matthews *et al.*, Global plate boundary evolution and kinematics since the late Paleozoic. *Global Planet Change* **146**, 226-250 (2016).
4. T. H. Torsvik *et al.*, Pacific-Panthalassic Reconstructions: Overview, Errata and the Way Forward. *Geochemistry, Geophysics, Geosystems* **20**, 3659-3689 (2019).
5. T. H. Torsvik *et al.*, Pacific plate motion change caused the Hawaiian-Emperor Bend. *Nature Communications* **8**, 15660 (2017).
6. I. H. Campbell, R. W. Griffiths, Implications of mantle plume structure for the evolution of flood basalts. *Earth Planet Sc Lett* **99**, 79-93 (1990).
7. S. E. Bryan, L. Ferrari, Large igneous provinces and silicic large igneous provinces: Progress in our understanding over the last 25 years. *GSA Bulletin* **125**, 1053-1078 (2013).
8. P. Glišović, A. M. Forte, On the deep-mantle origin of the Deccan Traps. *Science* **355**, 613-616 (2017).
9. P. R. Vogt, Subduction and Aseismic Ridges. *Nature* **241**, 189-191 (1973).
10. G. P. Avdeiko, D. P. Savelyev, A. A. Palueva, S. V. Popruzhenko, in *Volcanism and Subduction: The Kamchatka Region,* J. Eichelberger, E. Gordeev, P. Izbekov, M. Kasahara, J. Lees, Eds. (American Geophysical Union, 2007), pp. 37-55.
11. R. A. Duncan, R. A. Keller, Radiometric ages for basement rocks from the Emperor Seamounts, ODP Leg 197. *Geochemistry, Geophysics, Geosystems* **5**, (2004).
12. Y. L. Niu, M. J. O'Hara, J. A. Pearce, Initiation of subduction zones as a consequence of lateral compositional buoyancy contrast within the lithosphere: A petrological perspective. *J Petrol* **44**, 851-866 (2003).
13. B. Steinberger, C. Gaina, Plate-tectonic reconstructions predict part of the Hawaiian hotspot track to be preserved in the Bering Sea. *Geology* **35**, 407-410 (2007).
14. M. Portnyagin, D. Savelyev, K. Hoernle, F. Hauff, D. Garbe-Schonberg, Mid-Cretaceous Hawaiian tholeiites preserved in Kamchatka. *Geology* **36**, 903-906 (2008).
15. M. Cloos, Lithospheric buoyancy and collisional orogenesis: Subduction of oceanic plateaus, continental margins, island arcs, spreading ridges, and seamounts. *GSA Bulletin* **105**, 715-737 (1993).
16. G. Rossi, G. A. Abers, S. Rondenay, D. H. Christensen, Unusual mantle Poisson's ratio, subduction, and crustal structure in central Alaska. *Journal of Geophysical Research: Solid Earth* **111**, (2006).
17. C. R. Gans *et al.*, Continental and oceanic crustal structure of the Pampean flat slab region, western Argentina, using receiver function analysis: new high-resolution results. *Geophys J Int* **186**, 45-58 (2011).
18. P.-A. Arrial, M. I. Billen, Influence of geometry and eclogitization on oceanic plateau subduction. *Earth Planet Sc Lett* **363**, 34-43 (2013).
19. J. van Hunen, A. P. van den Berg, N. J. Vlaar, On the role of subducting oceanic plateaus in the development of shallow flat subduction. *Tectonophysics* **352**, 317-333 (2002).
20. L. Liu *et al.*, The role of oceanic plateau subduction in the Laramide orogeny. *Nat Geosci* **3**, 353-357 (2010).
21. F. M. Dávila, C. Lithgow-Bertelloni, Dynamic uplift during slab flattening. *Earth Planet Sc Lett* **425**, 34-43 (2015).
22. S. W. French, B. Romanowicz, Broad plumes rooted at the base of the Earth's mantle beneath major hotspots. *Nature* **525**, 95-99 (2015).
23. C. Lu, S. P. Grand, H. Y. Lai, E. J. Garnero, TX2019slab: A New P and S Tomography Model Incorporating Subducting Slabs. *J Geophys Res-Sol Ea* **124**, 11549-11567 (2019).
24. J. M. Lees *et al.*, in *Volcanism and Subduction: The Kamchatka Region,* J. Eichelberger, E. Gordeev, P. Izbekov, M. Kasahara, J. Lees, Eds. (AGU, Washington DC, 2007), pp. 65-75.
25. H. Kawakatsu, F. L. Niu, Seismic Evidence for a 920-Km Discontinuity in the Mantle. *Nature* **371**, 301-305 (1994).
26. L. Waszek, N. C. Schmerr, M. D. Ballmer, Global observations of reflectors in the mid-mantle with implications for mantle structure and dynamics. *Nat Commun* **9**, 385 (2018).

27. R. Maguire, J. Ritsema, S. Goes, Evidence of Subduction-Related Thermal and Compositional Heterogeneity Below the United States From Transition Zone Receiver Functions. *Geophys Res Lett* **45**, 8913-8922 (2018).
28. Materials and methods are available as supplementary materials on *Science* Online.
29. P. M. Shearer, Global Mapping of Upper-Mantle Reflectors from Long-Period SS Precursors. *Geophys J Int* **115**, 878-904 (1993).
30. N. Schmerr, C. Thomas, Subducted lithosphere beneath the Kuriles from migration of PP precursors. *Earth Planet Sc Lett* **311**, 101-111 (2011).
31. Z. Zheng, B. Romanowicz, Do double '*SS* precursors' mean double discontinuities? *Geophys J Int* **191**, 1361-1373 (2012).
32. L. Stixrude, C. Lithgow-Bertelloni, Thermodynamics of mantle minerals - II. Phase equilibria. *Geophys J Int* **184**, 1180-1213 (2011).
33. L. Stixrude, C. Lithgow-Bertelloni, Thermodynamics of mantle minerals - I. Physical properties. *Geophys J Int* **162**, 610-632 (2005).
34. W. B. Xu, C. Lithgow-Bertelloni, L. Stixrude, J. Ritsema, The effect of bulk composition and temperature on mantle seismic structure. *Earth Planet Sc Lett* **275**, 70-79 (2008).
35. L. Stixrude, C. Lithgow-Bertelloni, Geophysics of Chemical Heterogeneity in the Mantle. *Annual Review of Earth and Planetary Sciences, Vol 40* **40**, 569-595 (2012).
36. W. P. Richardson, E. A. Okal, S. Van der Lee, Rayleigh–wave tomography of the Ontong–Java Plateau. *Phys Earth Planet In* **118**, 29-51 (2000).
37. P. E. van Keken, S. Karato, D. A. Yuen, Rheological control of oceanic crust separation in the transition zone. *Geophys Res Lett* **23**, 1821-1824 (1996).
38. E. M. Syracuse, G. A. Abers, Global compilation of variations in slab depth beneath arc volcanoes and implications. *Geochem Geophy Geosy* **7**, Q05017 (2006).
39. P. Wessel, L. W. Kroenke, Ontong Java Plateau and late Neogene changes in Pacific plate motion. *Journal of Geophysical Research: Solid Earth* **105**, 28255-28277 (2000).
40. R. D. Müller *et al.*, Ocean Basin Evolution and Global-Scale Plate Reorganization Events Since Pangea Breakup. *Annu Rev Earth Pl Sc* **44**, 107-138 (2016).
41. P. V. Doubrovine, B. Steinberger, T. H. Torsvik, Absolute plate motions in a reference frame defined by moving hot spots in the Pacific, Atlantic, and Indian oceans. *Journal of Geophysical Research: Solid Earth* **117**, (2012).
42. M. Domeier *et al.*, Intraoceanic subduction spanned the Pacific in the Late Cretaceous–Paleocene. *Science Advances* **3**, eaao2303 (2017).
43. R. D. Müller *et al.*, GPlates: Building a Virtual Earth Through Deep Time. *Geochemistry, Geophysics, Geosystems* **19**, 2243-2261 (2018).
44. W. H. F. Smith, D. T. Sandwell, Global Sea Floor Topography from Satellite Altimetry and Ship Depth Soundings. *Science* **277**, 1956-1962 (1997).
45. P. Bird, An updated digital model of plate boundaries. *Geochem Geophy Geosy* **4**, (2003).
46. B. L. N. Kennett, E. R. Engdahl, R. Buland, Constraints on seismic velocities in the Earth from traveltimes. *Geophys J Int* **122**, 108-124 (1995).
47. B. L. N. Kennett, E. R. Engdahl, Traveltimes for Global Earthquake Location and Phase Identification. *Geophys J Int* **105**, 429-465 (1991).
48. S. S. Wei, P. M. Shearer, A sporadic low-velocity layer atop the 410 km discontinuity beneath the Pacific Ocean. *J Geophys Res-Sol Ea* **122**, 5144-5159 (2017).
49. B. Efron, R. Tibshirani, Statistical data analysis in the computer age. *Science* **253**, 390-395 (1991).
50. G. Laske, G. Masters., Z. Ma, M. Pasyanos, Update on CRUST1.0 - A 1-degree Global Model of Earth's Crust. *Geophys. Res. Abstracts, 15, Abstract EGU2013-2658*, (2013).
51. J. Ritsema, A. Deuss, H. J. van Heijst, J. H. Woodhouse, S40RTS: a degree-40 shear-velocity model for the mantle from new Rayleigh wave dispersion, teleseismic traveltime and normal-mode splitting function measurements. *Geophys J Int* **184**, 1223-1236 (2011).
52. C. Li, R. D. van der Hilst, E. R. Engdahl, S. Burdick, A new global model for P wave speed variations in Earth's mantle. *Geochem Geophy Geosy* **9**, (2008).

53. M. Obayashi *et al.*, Finite frequency whole mantle P wave tomography: Improvement of subducted slab images. *Geophys Res Lett* **40**, 5652-5657 (2013).
54. M. L. Amaru, Universiteit Utrecht, Utrecht (2007).
55. P. M. Shearer, M. P. Flanagan, M. A. H. Hedlin, Experiments in migration processing of *SS* precursor data to image upper mantle discontinuity structure. *J Geophys Res-Sol Ea* **104**, 7229-7242 (1999).
56. J. P. Watt, G. F. Davies, R. J. O'Connell, The elastic properties of composite materials. *Reviews of Geophysics* **14**, 541-563 (1976).
57. Z. Zhang, L. Stixrude, J. Brodholt, Elastic properties of MgSiO3-perovskite under lower mantle conditions and the composition of the deep Earth. *Earth Planet Sc Lett* **379**, 1-12 (2013).
58. T. Ishii, H. Kojitani, M. Akaogi, Phase Relations of Harzburgite and MORB up to the Uppermost Lower Mantle Conditions: Precise Comparison With Pyrolite by Multisample Cell High-Pressure Experiments With Implication to Dynamics of Subducted Slabs. *Journal of Geophysical Research: Solid Earth* **124**, 3491-3507 (2019).
59. T. Kubo *et al.*, Metastable garnet in oceanic crust at the top of the lower mantle. *Nature* **420**, 803-806 (2002).
60. T. Kubo *et al.*, Kinetics of the post-garnet transformation: Implications for density and rheology of subducting slabs. *Phys Earth Planet In* **170**, 181-192 (2008).
61. M. Nishi, T. Irifune, H. Ohfuji, Y. Tange, Intracrystalline nucleation during the post-garnet transformation under large overpressure conditions in deep subducting slabs. *Geophys Res Lett* **39**, (2012).
62. S. Stein, M. Wysession, *An Introduction to Seismology, Earthquakes, and Earth Structure*. (Blackwell Publishing, Malden, MA, 2003), pp. 308-309.